






The Imprint of Large-scale Structure on the Ultrahigh-energy Cosmic-Ray Sky

Chen Ding (丁忱)¹ , Noémie Globus^{1,2,3} , and Glennys R. Farrar¹ ¹ Center for Cosmology and Particle Physics, New York University, New York, NY 10003, USA; cd2209@nyu.edu, nglobus-visitor@flatironinstitute.org, g25@nyu.edu² Center for Computational Astrophysics, Flatiron Institute, Simons Foundation, New York, NY 10010, USA

Received 2021 January 24; revised 2021 March 12; accepted 2021 March 22; published 2021 May 24

Abstract

Ultrahigh-energy cosmic rays (UHECRs) are atomic nuclei from space with vastly higher energies than any other particles ever observed. Their origin and chemical composition remain a mystery. As we show here, the large and intermediate angular scale anisotropies observed by the Pierre Auger Observatory are a powerful tool for understanding the origin of UHECRs. Without specifying any particular production mechanism but only postulating that the source distribution follows the matter distribution of the local universe, a good accounting of the magnitude, direction, and energy dependence of the dipole anisotropy at energies above 8×10^{18} eV is obtained after taking into account the impact of energy losses during propagation (the “GZK horizon”), diffusion in the extragalactic magnetic field, and deflections in the Galactic magnetic field (GMF). This is a major step toward the long-standing hope of using UHECR anisotropies to constrain UHECR composition and magnetic fields. The observed dipole anisotropy is incompatible with a pure proton composition in this scenario. With a more accurate treatment of energy losses, it should be possible to further constrain the cosmic-ray composition and properties of the extragalactic magnetic field, self-consistently improve the GMF model, and potentially expose individual UHECR sources.

Unified Astronomy Thesaurus concepts: [Cosmic ray astronomy \(324\)](#); [Cosmic ray sources \(328\)](#); [Cosmic rays \(329\)](#); [Extragalactic magnetic fields \(507\)](#); [Milky Way magnetic fields \(1057\)](#); [Ultra-high-energy cosmic radiation \(1733\)](#); [Cosmic anisotropy \(316\)](#); [Large-scale structure of the universe \(902\)](#)

1. Introduction

Cosmic rays are atomic nuclei that travel through space at almost the speed of light. The existence of cosmic rays of energy beyond 10^{20} eV (100 EeV) has been known for nearly 60 yr (Linsley 1963), but their origin and composition are still an enigma. The fact that cosmic rays are deflected on their way to the Earth by the extragalactic and Galactic magnetic fields (EGMF and GMF) makes it difficult to pinpoint their sources. Two observatories, the Pierre Auger Observatory (Abraham et al. 2004) and the Telescope Array (TA; Kawai et al. 2008), have made great efforts during the last decade in measuring the energy spectrum, composition, and arrival direction of ultrahigh-energy cosmic rays (UHECRs).

A breakthrough in UHECR astrophysics came in 2017, when the Pierre Auger Observatory reported the first anisotropy to pass the 5σ discovery threshold: a dipole with an amplitude of $6.5^{+1.3}_{-0.9}\%$, with a direction that points far away from the Galactic center (Aab et al. 2017a, 2020a) and an intensity that increases with energy (Aab et al. 2018a, 2020a). Auger and TA have also reported observations of anisotropies on intermediate angular scales, with a hot spot above 37 EeV reported by Auger at a 3.9σ significance level and a hot spot above 57^4 EeV reported by TA at 2.9σ (Kawata et al. 2020). Such observations offer a great opportunity for investigating the origin of UHECRs.

Before presenting our hypothesis, we remind the reader how the perspective on UHECR origins has evolved. In early days, it was assumed that UHECRs were protons, and that magnetic deflections would not be more than a few degrees, so unless

individual sources were so weak as to typically contribute zero to one event to the data set, sources could be identified by clusters of events (Hayashida et al. 1996). This picture was dislodged due to the absence of significant small-scale clustering as statistics increased and direct evidence from Auger that protons account for a small fraction of UHECRs ≥ 8 EeV (see Allard 2012 for a contemporaneous review). Lack of small-scale clustering could be due to a high source density or larger magnetic deflections associated with the higher Z of heavier nuclei; thus, a low source density may still be allowed.

We adopt here the simplest possible starting hypothesis: the UHECR source distribution follows the large-scale structure (LSS) of the universe. This must be valid, generally with some bias factor, unless UHECR sources are so rare and powerful that stochastic effects outweigh the mean distribution. The idea of using UHECRs to probe the LSS of the universe was proposed by Waxman et al. (1997; see also Alhers et al. 2017, for a more recent account). Thanks to work by cosmologists (Courtois et al. 2013; Hoffman et al. 2018), the LSS is well enough known up to a few hundred megaparsecs that we can take it as an input in our model.

The UHECR arrival direction pattern is influenced not only by the source distribution but also by energy losses and photodisintegration reactions during propagation (Greisen 1966; Zatsepin & Kuzmin 1966) and deflections in the EGMFs and GMFs. The main uncertainties in predicting the UHECR anisotropy for a given source hypothesis come from our limited knowledge of the EGMFs and GMFs and our lack of understanding of hadronic physics that leads to uncertainty on the cosmic-ray composition. We allow for these uncertainties via parameters in our modeling.

We continue the line of work initiated in Globus & Piran (2017) and Globus et al. (2019b), with three key advances. First, we account for deflections in the GMF that significantly

³ Current address: ELI Beamlines, Institute of Physics, Czech Academy of Sciences, 25241 Dolní Brezany, Czech Republic; noemie.globus@eli-beams.eu.

⁴ Note that there is evidence of an offset in the Auger and TA energy scales, such that 57 EeV for TA corresponds to ~ 43 EeV for Auger (Biteau et al. 2019).

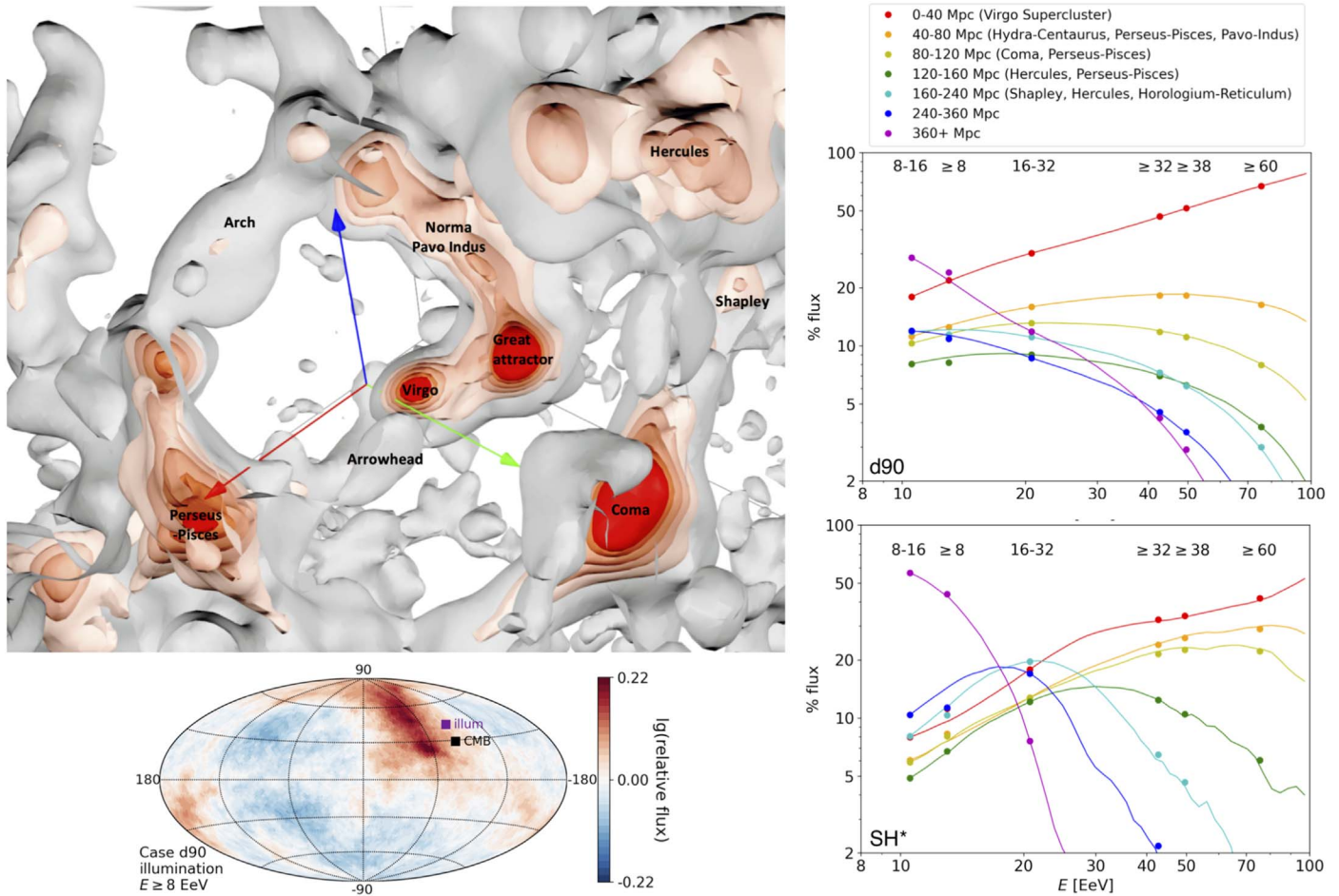


Figure 1. Top left: density field of the local universe derived from CosmicFlow-2 (Hoffman et al. 2018) in supergalactic coordinates; a 3D interactive view is available at <https://sketchfab.com/3d-models/quasi-linear-construction-of-the-density-field-91448f58ed5b4a30b5dc270a34fb4352>. Bottom left: intensity map of the flux illuminating the Galaxy ≥ 8 EeV for sources following the CosmicFlow-2 density field using the “exponential attenuation” treatment. The pattern is virtually identical for the “sharp cutoff” but with a maximum relative flux = 1.47 instead of 1.67 as in “exponential attenuation.” The direction of the dipole component is not far from the CMB dipole. In the right panels, the colored lines are the percentage contribution to the observed UHECR flux coming from the indicated distance bins as a function of energy for the parameters of the best-fitting d90 (top) and SH* (bottom) models detailed in Table 1. The dots represent the average over the energy bin indicated at the top. The actual calculation uses 1 Mpc bins in distance and 0.2 bins in $\log_{10}(E)$.

change both the magnitude and direction of the dipole anisotropy (bringing both into much better agreement with observations).⁵ Second, we systematically treat composition uncertainties, and third, we explore the limitations of the “sharp cutoff” treatment of Globus & Piran (2017) and Globus et al. (2019b) and take the first steps toward a full, accurate analysis.

In this Letter, we show that the observed dipole anisotropy and its evolution with energy ≥ 8 EeV are nicely explained as a signature of the local large-scale distribution of matter deflected by GMFs. This good accounting is obtained if UHECRs have a mixed composition—consistent with Auger measurements—but cannot be explained if UHECRs ≥ 8 EeV are predominantly protons. These are robust conclusions, as they are based on an improved treatment of energy losses during propagation, superseding the sharp cutoff treatment of Globus & Piran (2017) and Globus et al. (2019b), which assumed no energy loss out to a “horizon distance” and then no transmission beyond. Our studies suggest that with still more accurate treatments in the future, it should be possible to use

anisotropies on large and intermediate scales to simultaneously constrain the composition and potentially improve GMF modeling, as will be elaborated below. This delineates a future research program with ample rewards.

2. Elements of the Analysis

2.1. Source Distribution Model

We assume that the spatial distribution of UHECR sources follows the matter density distribution, and that all sources are “standard candles” in terms of luminosity, energy spectrum, and composition. We refer to this as the “LSS model.” As in Globus et al. (2019b), we use the LSS matter density field (Hoffman et al. 2018) derived from the CosmicFlows-2 catalog of peculiar velocities (Tully et al. 2014). The 3D distribution of LSS in our local universe is shown in Figure 1. With a distance of ~ 17 Mpc, the Virgo cluster produces a strong excess in the illumination map (IM; the map of flux illuminating the surface of the Milky Way) in a direction close to the Galactic north pole. The Virgo cluster is part of the Local Supercluster, which contributes most of the excesses within ~ 40 Mpc (Tully et al. 2013; Pomarède et al. 2020). Beyond the Local Supercluster,

⁵ Globus et al. (2019b) took a preliminary look at the impact of deflections by tracking 2×10^5 particles for a single rigidity and coherence length.

the northern sky is dominated by the Hydra-Centaurus, Coma, Hercules, and Shapley superclusters, while the southern sky is dominated by the Perseus-Pisces and Horologium-Reticulum superclusters. The further the distance, the more isotropic the universe appears, because a given solid angle corresponds to a larger volume of space to average over.

2.2. Extragalactic Energy Loss and Magnetic Diffusion

To take into account the horizon effects, we consider two approaches.

1. In the “sharp cutoff” approach of Globus et al. (2019b), a cosmic ray is taken to originate with uniform probability from any distance up to a fixed horizon, $H(A, E)$, where A is the mass number. The sources beyond horizon do not contribute to the flux received at Earth. With no EGMF, the horizon is taken to be the energy attenuation length, χ_{loss} , also denoted d_{GZK} (Globus et al. 2019b). Diffusion in the EGMF extends the path length beyond the linear distance to the source, and in the presence of an EGMF, the horizon is taken to be $\sqrt{d_{\text{diff}} d_{\text{GZK}}}$, where d_{diff} is the magnetic diffusion length. For specifics, see Globus et al. (2019b) and Appendix A. In the following, we refer to this as the “sharp cutoff” treatment.
2. In our more realistic exponential attenuation treatment, the contribution of a shell at a distance z is weighted in its contribution to the observed spectrum in proportion to the factor

$$\exp[-\ln(10) p(z, d_{\text{diff}})/d_{90}(A, E)], \quad (1)$$

where $p(z, d_{\text{diff}})$ is the mean path length accumulated during traversal of the linear distance z , and $d_{90}(A, E)$ is the distance within which 90% of the parent nuclei of UHECRs in composition bin A and energy above E originated. Since our explorations of EGMF diffusion using the “sharp cutoff” treatment favor a low or negligible EGMF impact, as discussed below, we restrict ourselves here to taking $p(z, d_{\text{diff}}) \rightarrow z$. In the following, we refer to this as the “exponential attenuation” treatment. It should be noted that this is not an exact description because the energy loss rate evolves during propagation in a nontrivial way as the composition and energy change; a differential description of the evolution in $\{A, E\}$ space would be more accurate. Moreover, even if the mean treatment of Equation (1) is an adequate approximation, the spectrum and composition at the source location should be treated as unknown and varied as part of the fitting procedure, the spectral and composition sensitivity being reflected in the fact that $d_{90}(A, E)$ depends on these. Aab et al. (2017b) provided the best current combined fit to the spectrum and composition at the source but did not provide the corresponding tables of $d_{90}(A, E)$. We use $d_{90}(A, E)$ from Globus et al. (2008), which is the most suitable compilation we could find in the literature; it is based on a spectral index of -2.4 , similar to one of the minima found in Aab et al. (2017b). Given the sensitivity of the Aab et al. (2017b) best-fit spectral parameters to the hadronic interaction model (HIM) used for analyzing the composition, the source spectral index must currently be considered quite uncertain. Happily, as discussed in

Appendix A.3, the analysis is relatively insensitive to this uncertainty.

For either treatment of propagation, we adjust the cumulative contribution of all of the distance shells for each energy and composition bin to match the observed spectrum at Earth (Aab et al. 2020b, 2020c).

We explore the possible spreading of the source images and reduction in horizon due to diffusion in the EGMF using the sharp cutoff treatment. We adopt the simplest hypothesis that the universe is filled with homogeneous and isotropic turbulent magnetic fields. While the turbulence level of the EGMF is still unknown, upper limits obtained by various measurements or arguments exist (Durrer & Neronov 2013). We adopt a Kolmogorov spectrum, and—to fully cover the possible parameter space—we consider an rms random field strength $0.08 \text{ nG} \leq B_{\text{EG}} \leq 10 \text{ nG}$ and coherence length $0.08 \text{ Mpc} \leq \lambda_{\text{EG}} \leq 0.5 \text{ Mpc}$. The diffusion coefficient, D_{EG} , and indeed all magnetic deflections, depends on rigidity, E/Z ; in the relevant rigidity domain, D_{EG} is proportional to $(E/Z B_{\text{EG}} \lambda_{\text{EG}}^{0.5})^2$ (Globus et al. 2008). The intensity profile of a single source depends on the diffusion coefficient and the distance to the source; it is calculated by a method following the diffusion of light in scattering media that allows one to take into account the transition between quasi-linear and diffusive regimes, as detailed in Appendix A.

For a given assumed EGMF, composition, and energy, and adopting either the “sharp cutoff” or “exponential attenuation,” we calculate the weight of a 1 Mpc thick shell of matter at distance z in the total observed cosmic-ray flux at the given (A, E) . The final IM for that (A, E) and attenuation model is then the weighted sum of the surface mass density in each shell. To enable the reader to visualize how different distances contribute, the left column of Figure 2 shows the surface density contrast of the three nearest 40 Mpc thick layers of the nearby universe. After weighting by the attenuation factor, one gets the contribution of the shell to the IM. The middle and right columns should be ignored for now; they show contributions to the arrival direction maps and will be discussed later.

2.3. Galactic Propagation

Once extragalactic cosmic rays enter the Galaxy, they are deflected by the GMF, which has a complex geometry and includes both ordered (coherent) and turbulent (random) magnetic fields. The Jansson & Farrar (2012, hereafter JF12) model is the leading GMF model available at this time. It is constrained by some 40,000 Faraday rotation measures (RMs) of extragalactic sources and polarized and unpolarized synchrotron emission as inferred by the Wilkinson Microwave Anisotropy Probe (WMAP). The JF12 model allows for a coherent and/or turbulent poloidal (X-shaped) halo field inspired by the field geometry seen in external galaxies. (See Farrar 2014 and Appendix C for a discussion of other GMF models, the limitations of JF12, and references.) The unexpected finding of JF12 was that the X-field is actually a directed poloidal field extending from south to north. In addition to the X-field, JF12 incorporated spiral arms and a toroidal halo and allowed for the presence of anisotropic random magnetic fields.

To model the propagation of UHECRs through the Galaxy, we use high-resolution particle tracking (1.8 billion trajectories) from Farrar & Sutherland (2019) in the JF12

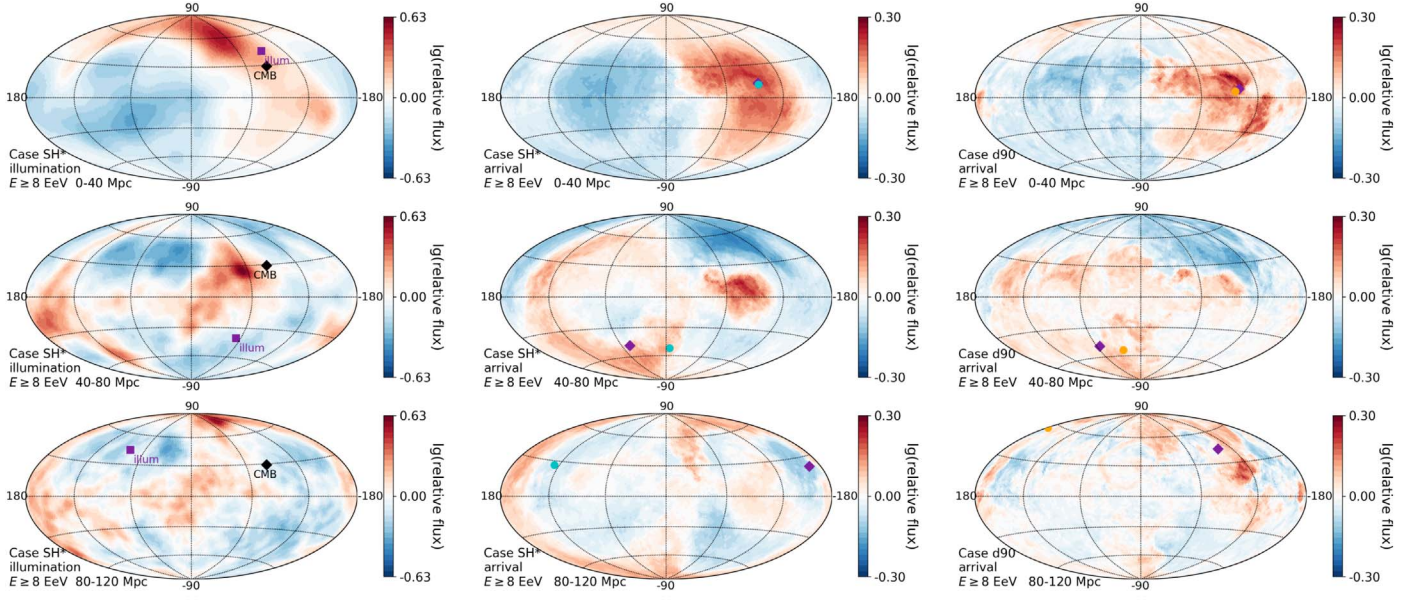


Figure 2. Surface density maps (left column) and arrival maps after propagation in the JF12 GMF model for the SH* (middle) and d90 (right) attenuation models in LSS shells covering distances of (top to bottom) 0–40, 40–80, and 80–120 Mpc. The maps here are for $E \geq 8$ EeV; plots including $E \geq 32$ EeV and a more complete set of distances and models are given in Appendix E, Figures E1–E4.

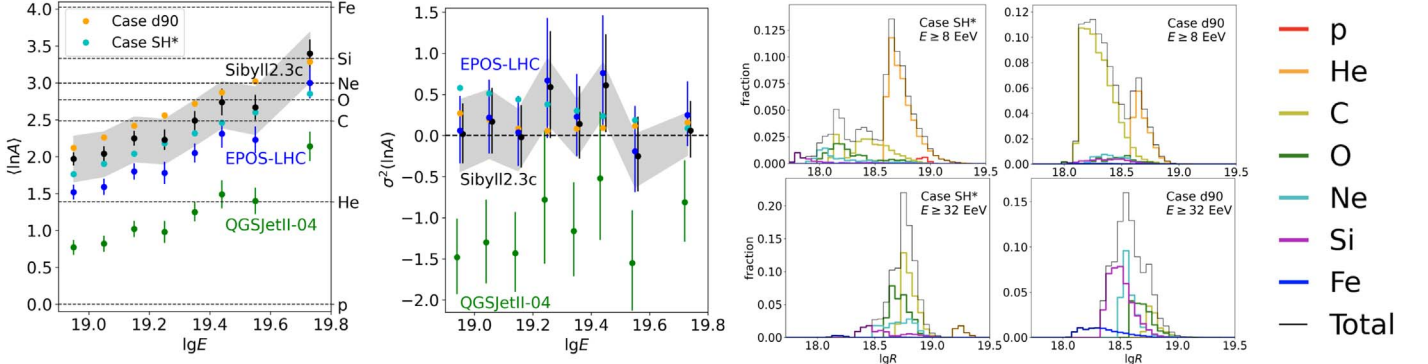


Figure 3. Composition observables from shower development data. Left and middle panels: evolution with energy of $\langle \ln A \rangle$ and $\sigma^2(\ln A)$ with the statistical error, inferred using Sibyll2.3 c (black), EPOS-LHC (blue), and QGSJETII-04 (green) from Yushkov (2019). The shaded bands mark the systematic error for Sibyll2.3 c; the other two interaction models have similar systematic errors. The cyan dots show our overall best fit to the dipole, hot spot, and composition for the sharp-cutoff family of modeling, SH*, while the orange dots are the best fit for exponential attenuation modeling, with just dipole and composition being fit. Right panels: corresponding rigidity spectrum for the data set ≥ 8 (top) and ≥ 32 (bottom) EeV for the SH* (left) and d90 (right) analyses.

coherent+random GMF model. This procedure captures deflection, diffusion, and magnification and demagnification effects (Farrar & Sutherland 2019). The coherence length of the GMF is not constrained by the JF12 or other GMF modeling, but it is commonly thought to be 30–100 pc in the bulk of the volume (Farrar 2014). With that in mind, Farrar & Sutherland (2019) provided trajectories for $\lambda_{\text{coh}} = 30$ and 100 pc. Given these high-resolution simulated trajectories, the maps of flux at Earth can be calculated from the IMs (see Appendix B.1). In order to have more choices of effective GMF coherence lengths λ_G , we mix the trajectories of 30 and 100 pc with different weights to interpolate between them.

2.4. Mass Composition

The mass composition of UHECRs can be inferred from measurements of the longitudinal development of UHE air showers with the use of HIMs. Figure 3 shows the mean and variance of $\ln A$ and their uncertainties in eight energy bins as inferred by the Pierre Auger Collaboration (Yushkov 2019)

using three different HIMs: Sibyll2.3 c, EPOS-LHC, and QGSJETII-04.⁶ We parameterize the evolution of the composition with energy as follows (abbreviating $\log_{10}(E) \equiv \lg E$):

1. $\langle \ln A \rangle = \alpha \lg E + \langle \ln A \rangle_{8\text{EeV}}$ and
2. $\sigma^2(\ln A) = \beta \lg E + \sigma^2(\ln A)_{8\text{EeV}}$.

Thus, the model composition is characterized by four parameters, $\Omega \equiv \{\alpha, \beta, \langle \ln A \rangle_{8\text{EeV}}, \sigma^2(\ln A)_{8\text{EeV}}\}$.⁷ We consider seven chemical elements, p, He, C, O, Ne, Si, and Fe, to reduce the unphysical discontinuities for low A and mix them with appropriate proportions to achieve the $\langle \ln A \rangle$ and $\sigma^2(\ln A)$ specified by a given choice of Ω (see Appendix D for details.) The relative abundances of the seven chemical elements in the ≥ 8 and ≥ 32 EeV bins as a function of their rigidity ($R = E/Z$)

⁶ It should be noted that QGSJETII-04 gives an unphysical $\sigma^2(\ln A)$.

⁷ For the purpose of reporting results, we quote a different $\Omega \equiv [\langle \ln A \rangle_{8-10\text{EeV}}, \langle \ln A \rangle_{\geq 40\text{EeV}}, \sigma^2(\ln A)_{8-10\text{EeV}}, \sigma^2(\ln A)_{\geq 40\text{EeV}}]$ because it corresponds to X_{max} measurements (the first and last data points in Figure 3, left and middle panels). The two Ω s are equivalent and can be used interchangeably.

Table 1
Summary of Model Parameters and Results

Cases		Iso	SH*	SH _E *	SH	d90	d90*	Pure Proton (PP)
Model	Source	Isotropic	LSS	LSS	LSS	LSS	LSS	LSS
	Distance weighting	...	Sharp	Sharp	Sharp	Exponential	Exponential	Exponential
	HIM	Sibyll2.3c	Sibyll2.3c	EPOS-LHC	Sibyll2.3c	Sibyll2.3c	Sibyll2.3c	...
Likelihood	$\ln L(\text{dipole} \Theta; \text{source})$	-3.4	14.5	13.8	20.6	13.4	10.2	-6.0
	$\ln L(\text{events} \Theta; \text{source})$	0 (Ref)	11.1	10.9	2.4 [†]	0.1 [†]	4.4	0.6 [†]
	$\ln L(\langle \ln A \rangle \Omega; \text{HIM})$	4.4	4.0	3.8	1.8	4.1	3.5	...
	$\ln L(\sigma^2(\ln A) \Omega; \text{HIM})$	-2.8	-3.3	-3.7	-3.0	-3.0	-3.9	...
	Sum of three $\ln L$ s without $\ln L(\text{events})$	-1.9	15.3	13.8	19.5	14.4	9.8	...
	Sum of four $\ln L$ s (Equation (2))	-1.9	26.3	24.7	21.8	14.5	14.2	...
Best-fit parameters	$\lg D_{\text{EG},5\text{EV}}$...	$2.79^{+0.60}_{-0.20}$	$2.79^{+0.60}_{-0.20}$	$2.39^{+0.40}_{-0.40}$	∞	∞	∞
	$\lg \lambda_G$...	$1.58^{+0.10}_{-0.08}$	$1.58^{+0.13}_{-0.08}$	$1.82^{+0.13}_{-0.16}$	1.95	1.66	1.48
	$\langle \ln A \rangle_{8-10 \text{ EeV}}$	2.02	$1.76^{+0.19}_{-0.15}$	$1.64^{+0.18}_{-0.16}$	$2.11^{+0.36}_{-0.29}$	2.12	2.27	0
	$\langle \ln A \rangle_{\geq 40 \text{ EeV}}$	3.19	$2.87^{+0.17}_{-0.10}$	$2.84^{+0.13}_{-0.08}$	$3.27^{+0.33}_{-0.30}$	3.29	3.44	0
	$\sigma^2(\ln A)_{8-10 \text{ EeV}}$	0.31	$0.48^{+0.27}_{-0.20}$	$0.47^{+0.27}_{-0.24}$	$0.40^{+0.30}_{-0.18}$	0.27	0.23	0
	$\sigma^2(\ln A)_{\geq 40 \text{ EeV}}$	0.19	$0.09^{+0.32}_{-0.05}$	$0.09^{+0.34}_{-0.05}$	$0.28^{+0.28}_{-0.19}$	0.16	0.62	0
	B_{EG} if $\lambda_{\text{EG}} = 0.2 \text{ Mpc}$...	$0.32^{+0.08}_{-0.16}$	$0.32^{+0.08}_{-0.16}$	$0.50^{+0.13}_{-0.25}$	0	0	0
Hot spot	Number of events in 27° circle centered at (309°7, 17°4). Obs = 188	125^{+11}_{-11}	154^{+12}_{-11}	156^{+12}_{-12}	135^{+11}_{-11}	139^{+11}_{-11}	138^{+11}_{-11}	160^{+12}_{-12}
	Li–Ma significance in 27° circle centered at (309°7, 17°4). Obs = 5.6	$0.0^{+1.0}_{-1.0}$	$2.7^{+1.1}_{-1.0}$	$2.8^{+1.1}_{-1.1}$	$0.9^{+1.0}_{-1.0}$	$1.3^{+1.0}_{-1.0}$	$1.2^{+1.0}_{-1.0}$	$3.2^{+1.0}_{-1.1}$

Note. In cases SH*, SH_E*, and SH, the sharp cutoff horizon is used, while for the remainder of the examples, the exponential attenuation weighting of Equation (1) is used. The best-fit parameters are shown as the median with 1σ confidence levels (i.e., 16th and 84th percentiles). The SH cases allow for an EGMF, while the EGMF is set to zero for the rest. For SH and d90, only the dipole and composition are fit, while for the cases with asterisks in their names, the events above 38 EeV are also included in the fit. For the pure proton case, “PP,” only the dipole (not the composition or events) is fit. Note that the total $\ln L$ should only be compared between cases where the same data sets are being fit. Entries in the $\ln L$ section marked with a dagger (†) indicate that the corresponding data were not included in the fitting for that case. In the bottom two rows, the hot-spot results are calculated from millions of mock data sets generated from the model arrival map above 38 EeV with the best-fit parameters. The confidence level represents the statistical uncertainty in the mock data sets and does not represent the uncertainty due to the uncertainty in the best-fit parameters.

are displayed in the right panel of Figure 3 for the two overall best-fitting SH* and d90 models.

2.5. Fitting Model Parameters

In this analysis, we fit the parameters of the model described above to the following observations or subsets of them.

Nine dipole components d_x , d_y , d_z reported by Auger in the three energy bins 8–16, 16–32, and ≥ 32 EeV (Aab et al. 2020a), denoted “dipole” below.

The observed arrival directions of 1288 events above 38 EeV observed by Auger, reconstructed from the Li–Ma sky map in Caccianiga (2019), denoted “events” below.

The $\langle \ln A \rangle$ and $\sigma^2(\ln A)$ inferred by Auger from X_{max} measurements in the eight energy levels ≥ 8 EeV, for each HIM (Yushkov 2019).

The quality of the fit is given by the likelihood of obtaining the given measurements if the cosmic-ray intensity maps and composition are given by the LSS model for any specified parameter set. For instance, when fitting all three sets of data listed above, the likelihood function is

$$\ln L \equiv \ln L(\text{dipole}|\Theta; \text{source}) + \ln L(\text{events}|\Theta; \text{source}) + \ln L(\langle \ln A \rangle |\Omega; \text{HIM}) + \ln L(\sigma^2(\ln A) |\Omega; \text{HIM}), \quad (2)$$

where “source” is the specified source distribution model (LSS or isotropic and treatment of attenuation), “HIM” refers to the HIM used to infer the composition, and Θ is the set of six parameters to optimize the fit: two parameters for the EGMF and GMF ($D_{\text{EG},5\text{EV}}$ and λ_G) and the four composition parameters denoted by Ω .

3. How Good Is the LSS Ansatz?

We have performed various studies of the LSS ansatz using the framework described in the previous section and fitting to more or less data. The results for some instructive cases are reported in Table 1. The column “Iso” shows the analysis applied to an isotropic sky map weighted by the Auger exposure, while subsequent columns are for the LSS source hypothesis, exploring different treatments of the attenuation (sharp for cases labeled SH and exponential for the rest) and composition (fitting to Sibyll2.3c or EPOS-LHC, or simply pure proton (PP)). Cases labeled with an asterisk denote that the parameters of the model have been fit to the events above 38 EeV and not just the nine dipole components. A discussion of the lessons learned is given below.

The six “Likelihood” rows of Table 1 give the log-likelihood for each case, broken down by data sets, and the total. In each case, the $\ln L$ values for data sets not included in the fit are marked by a dagger. Note that the larger the $\ln L$, the better the

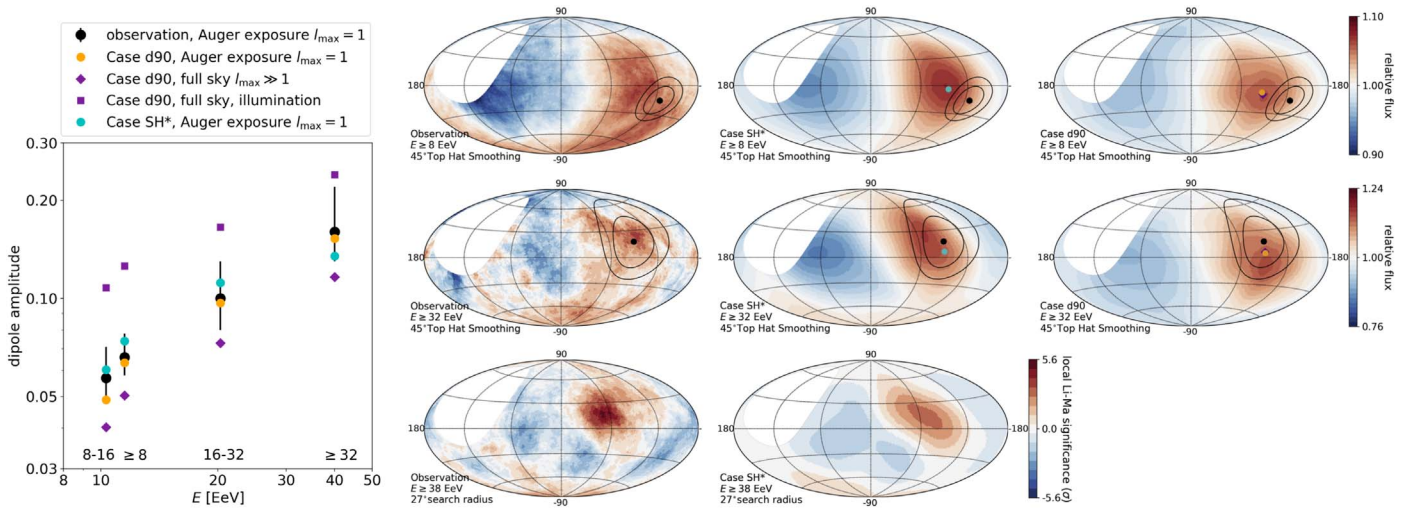


Figure 4. Comparison between observed and model anisotropy. In the left panel, the magnitude of the LSS-induced dipole amplitude for different energy bins is compared to the data (black dots with error bars). The orange and cyan dots show the prediction for the d90 and SH* models given Auger’s exposure. For comparison, the purple diamonds show the d90 prediction with full-sky exposure, and the purple squares show the prediction without GMF processing; see Table E2 in Appendix E for the full set of dipole components. The left column of sky maps shows the Auger data maps from Aab et al. (2017a, 2018a) and Caccianiga (2019). The top-hat maps from Aab et al. (2017a, 2018a) are replotted using the same smoothing method as for the model maps as detailed in Section B.3. The closed black curves show the 68% and 95% confidence level regions of dipole direction, with the black dot indicating the center. The middle (right) columns show the SH* (d90) predictions; note that, sampled with the same number of events as in the data maps, the predicted LSS maps are similarly blotchy as the data maps. Top (middle) row: ≥ 8 EeV (≥ 32 EeV), smoothed by a 45° top hat for comparison to the Auger sky maps. The colored dot is the dipole direction of the model, reconstructed with detector exposure and $l_{\max} = 1$; the purple diamond is the dipole direction for full-sky exposure and $l_{\max} \gg 1$. Bottom row: Li–Ma significance above 38 EeV with a search radius of 27° for Auger (left) and the SH* model (middle).

fit. The next six rows give the best-fit parameters and their 68% confidence level range, and in the following row, we convert the EGMF constraint on $D_{EG,5EV}$ into more familiar terms by quoting the B_{EG} derived from $D_{EG,5EV}$ taking $\lambda_{EG} = 0.2$ Mpc. The final rows give “predictions” for the Auger hot spot in each case. Note that cases SH* and d90* include the events above 38 EeV as a constraint, so they naturally give better fits to the data above 38 EeV than the other cases.

At various points in this Letter, we have adopted models d90 and SH* to illustrate different points because d90 or d90* use the most realistic treatment of attenuation available now, and SH* gives the overall best fit. We select d90 rather than d90* because only fitting the dipole is most conservative, given that the events above 38 EeV may get a significant contribution from individual sources; moreover, the fit quality of d90 and d90* are similar. Conclusions that emerge independently of the horizon treatment (sharp cutoff versus exponential) can be taken to be robust and likely to endure in a more comprehensive study. We discuss below what these conclusions are and which questions need a more refined analysis to decide.

3.1. Extragalactic Magnetic Field

So far we have only explored the impact of the EGMF on the SH approach. There, the inferred EGMF is very small ($0.32^{+0.08}_{-0.16}$ or $0.50^{+0.13}_{-0.25}$ nG), depending on whether the model is fit to all of the data, including the events above 38 EeV (SH*), or not (SH). Either value is compatible with typical expectations in the homogeneous EGMF approximation and implies a lower impact of the EGMF on the anisotropy than would be obtained for the 10 nG used for the examples in Globus et al. (2008). We remark in passing that locally strong fields such as observed in massive galaxy clusters will concentrate UHECRs near their sources, effectively increasing the apparent source contrast. Near-future studies of source

“bias” with respect to the (predominantly dark) matter distribution will probably find the two effects quite degenerate.

3.2. Sensitivity to HIM

Cases SH* and SH_E* are the same, except that the first case fits the Auger composition inferred by taking Sibyll2.3 c as the HIM, and the second one uses the EPOS-LHC composition. The two cases are nearly identical in fit quality and inferred parameters; we adopt Sibyll2.3 below, since it is slightly preferred. Figure 3 shows that the best-fitting composition parameterizations found for cases d90 and SH* are quite consistent with the Auger composition results.

3.3. Dipole Anisotropy Predictions

Figure 4 summarizes the LSS model predictions for the dipole anisotropy and its energy dependence. The left panel of Figure 4 shows that the observed magnitude of the dipole amplitude and its energy evolution can be well described by the LSS model. As can be seen from Table 1, the overall quality of the fit is marginally better for SH* than for the d90 treatment, and better still for SH, which does not fit to the events. The best-fitting composition changes from SH* to d90 but without changing the quality of the fit to the composition data. In principle, the exponential attenuation model should be more accurate than the sharp cutoff models, but, as noted above, the source spectral index of -2.4 underlying the $d_{90}(A,E)$ values may not be the optimal representation of the spectrum, and the energy-averaged character of the present treatment (Equation (1)) is only a first approximation.

The right panels of Figure 4 show the observed sky maps compared to the SH* and d90 model predictions for the arrival maps for the energy bins ≥ 8 and ≥ 32 EeV (and the Li–Ma map above 38 EeV, discussed below). Unlike the observation sky map ≥ 8 EeV, the sky above 32 EeV does not look like a simple

dipole. It has two distinct regions of excess, one in the northern sky and another toward the Galactic south pole. The LSS model gives a reasonable explanation for this. The increase of energy threshold results in the decrease of horizon size, which in turn leads to a substantial increase in the percentage of flux from the Local (Virgo) and Hydra-Centaurus superclusters that give excess to the northern sky. It also increases the percentage of flux from the Perseus-Pisces supercluster, which, after processing by the GMF, gives regions of excess as seen in the southern hemisphere. These effects can be seen in Figure 2. The pattern of excess seen in Figure 4 is evocative of the pattern from Perseus-Pisces (after GMF deflections) and suggests that an improved treatment of attenuation could lead to a somewhat stronger contribution from the Perseus-Pisces region and enable a better fit the Auger observations ≥ 32 EeV.

3.4. Dipole Anisotropy Discussion

As already mentioned, in the LSS model, the observed UHECR dipole anisotropy is the result of an interplay between composition-dependent horizon and rigidity-dependent deflection/diffusion in the GMF. Energy loss processes should be well determined from laboratory measurements (but see Alves Batista et al. 2015), so if the matter distribution is sufficiently well known, anisotropies can contribute to disentangling composition and GMF, since they impact the arrival direction maps differently. Some sensitivity to EGMF diffusion may also be possible, as discussed earlier.

The left column of Figure 2 shows the surface density contrast of individual 40 Mpc shells out to 120 Mpc. In the absence of EGMF diffusion, the IMs (shown in Figure 1 and Appendix E) are superpositions of the surface density of 1 Mpc shells depending on attenuation and composition. All of the shells out to 360 Mpc are shown in Appendix E. One sees, as expected, that more distant shells that average over a larger volume show less contrast. Also shown in Figure 2 are the arrival direction maps corresponding to the given shells after deflection and diffusion in the GMF, as predicted by the d90 and SH* models for the $E \geq 8$ data set. Shells for more models extending to larger distances and including the ≥ 32 EeV predictions are shown in Figures E1–E4. For a given model, the arrival maps for the different energy thresholds have quite a similar pattern, due to the fact that the peak of the rigidity distributions changes rather little with threshold, as seen in the left panel of Figure 3 and expected for magnetic acceleration and energy losses preserving E/A , except for protons. Thus, the dominant reason that the direction and character of UHECR anisotropies change with energy is the horizon effect. In addition, as energy increases and the horizon is reduced, stochastic “cosmic variance” effects become more important, since the number of sources being sampled is reduced.

Setting aside this cosmic variance for our initial study, let us look more closely at how the relative contribution of flux from different distances in the nearby universe depends on energy, shown in Figures 1 and A3. For example, in the sharp-cutoff approximation, the Local Supercluster contributes 8% of the total UHECR flux for 8–16 EeV and 33% above 32 EeV; the corresponding numbers of the d90 model are 19% and 48%. The difference between attenuation treatments emphasizes the need to correctly model the attenuation, but the commonality underscores two main consequences of the LSS model for the

anisotropy: the dipole amplitude increases with energy, and the anisotropy pattern changes with energy.

The composition affects the anisotropy in two distinct ways.

(i) *The GMF deflections and dispersion are rigidity-dependent and generally increase as the rigidity drops.*

The d90 model favors a heavier composition than the SH* model, and as a result, its arrival maps look quite different. In Appendix E, we test a special model “d90sp” that uses the same exponential attenuation as d90, but uses the same composition as SH*. The comparison of illumination maps and arrival maps between d90 and d90sp illustrates the composition effect. A more extreme example is the pure proton model shown in Figure E4, for which the deflection provided by the GMF is far too small to be consistent with the observed dipole. Note that a possible EGMF would only affect the amplitude and not improve the direction of the dipole, so our not allowing for an EGMF does not limit the validity of this conclusion.

The impact of the energy threshold on GMF deflections for a single model can be seen in comparing the middle and right columns of the entire set of Figures E1–E4 in Appendix E. Possibly nonintuitively, the main impact is on the degree of contrast, because to first approximation, the mean rigidity that determines where the structures are does not change with rigidity threshold. However, the spread in rigidities and hence degree of smearing increases at lower energies due to the larger jumps between A values.

(ii) *The weight of different shells at a given energy is different for each A due to the A -dependence of energy loss lengths.* We assay the importance of this effect by comparing the illumination and arrival maps of d90 and d90sp models in Figures E2 and E3.

3.5. Intermediate-scale Anisotropies

As energy goes still higher, the separation of two regions of excess becomes even more noticeable. The arrival map above 38 EeV observed by Auger can be represented by a hot spot centered at (309°7, 17°4) in Galactic coordinates and an excess around the Galactic south pole. Auger found that the hot spot has the highest Li–Ma significance (Li & Ma 1983) with a 27° angular radius. The local Li–Ma significance is 5.6σ , and the post-trial significance is 3.9σ (Caccianiga 2019). The last column of Figure 4 shows the Li–Ma map of events above 38 EeV from Auger (Caccianiga 2019) and the predicted Li–Ma map from our case study SH*.

The SH* is fit to both the dipole and the events above 38 EeV to test whether the LSS alone, without a single source or sources, can give rise to the observed structure, as was hinted at by Globus et al. (2019b). To check the compatibility of an LSS model with hot-spot observations, we performed a hypothesis test using the same test statistic as in Aab et al. (2018b) and Abbasi et al. (2018) based on the log-likelihood ratio. The methodology is discussed in Appendix D. The test statistic $TS = 2 \ln L(\text{events}|\Theta; \text{source}) \approx 22$. By simulating mock data sets, we find that the isotropic model is disfavored against the SH* model by 4.8σ (see Appendix E.4).

The strength of the predicted LSS hot spot for our best-fitting description, case SH*, is weaker than the one observed. This could be the result of fitting to the arrival directions of all events above 38 EeV, which contain more information than just the strength of the hot spot, including the shape of the hot spot

and the south pole excess. To see whether a variation of the model parameters can give a similarly significant hot spot as observed, we carried out the exercise reported in the Table E1 column SH(Better Hot Spot)*, for which the objective function also includes the number of events inside the hot spot. The conclusion is that indeed, the hot spot can be readily described if it is included in the fitting without significant damage to the fit to dipole components and events above 38 EeV.

In the LSS model, both the hot spot and the south pole excess may be reflections of the LSS of the universe. In particular, for the SH* model, $\sim 40\%$ and $\sim 25\%$ of cosmic rays inside the hot spot come from the Local and Hydra-Centaurus superclusters, respectively, and these naturally lead to the observed structures after deflection in the GMF. It is important to note that the LSS models do not include specific galaxies, such as Cen A/NGC 4945/NGC 253. As shown in Aab et al. (2018b), individual classes of sources may instead be the origin of the hot spot and other structures seen above 38 EeV, if net GMF deflections are small enough. Auger also performed a correlation study with 2MRS galaxies as a proxy for local LSS; however, that study cannot be compared to the present one, because deflections in the GMF are ignored and 2MRS is a flux-limited catalog with a high flux threshold (K -band magnitude 11.75) and hence subject to greater cosmic variance issues than CosmicFlows-2.

We note that— independent of attenuation treatment and composition—no prominent structure in the direction of the TA hot spot is expected from the LSS. This can be seen in the all-sky prediction plots of Figures E1–E4. If the TA hot spot holds up as statistics increase, that would be strong evidence for an individual source not captured by the LSS treatment.

3.6. Composition

Conservatively applying the LSS analysis only to the dipole data, one sees from Table 1 cases d90 and SH* that roughly comparable, acceptable fits can be obtained for the different attenuation treatments, with the resulting best-fit compositions adjusting to give compatibility. This means that with good composition information—after HIM models are improved and vetted with future air shower development and accelerator observations—we can test the attenuation modeling in detail. Conversely, when more accurate attenuation modeling is in hand, LSS modeling of the dipole can constrain composition. The intermediate-scale anisotropies at higher energy are even more sensitive to composition and can provide important additional information, with self-consistency probably making it clear whether the Auger hot spot can be explained without a prominent individual source.

4. Summary and Conclusions

The postulate that the UHECR source distribution follows the matter distribution of the local universe, taking into account deflections in the GMF and possible diffusion in the EGMF, provides quite a good accounting of the magnitude, direction, and energy dependence of UHECR anisotropies ≥ 8 EeV.

A main feature of this LSS hypothesis is the horizon effect, a reduction of the observable UHECR universe with energy that leads to an increase of the contribution of nearby superclusters at the highest energies, whose contributions provide distinctive

signatures in the UHECR sky. The current implementation of the LSS model can account for the evolution of the observed dipole amplitude with energy, but, as can be seen in Figure 4, the LSS dipole direction for the ≥ 8 EeV bin is off by some degrees from the observed direction (95% confidence level circle). This can be due to our still-approximate treatment of the horizon effects, our incomplete knowledge of the local matter distribution, and/or our incomplete knowledge of the cosmic and GMFs. A refined GMF model is under development (Unger & Farrar 2019), and our knowledge of the LSS is evolving with new discoveries, such as the south pole wall (Pomarède et al. 2020), that are only partially taken into account in CosmicFlow-2, so we can reasonably expect better fidelity in the future.

Conclusions that can already be reached include the following.

1. The direction of the large-scale UHECR dipole and its evolution with energy appear to be the result of the interplay between the local large-scale matter distribution—especially the orientation of the Galaxy relative to the supergalactic plane—and deflection in the large-scale coherent poloidal (X-shaped) halo field of the Milky Way. Improvements in our understanding of the GMF can shift the predicted direction of the dipole some degrees, while the strength and orientation of the anisotropy arriving at the Galaxy is mainly sensitive to the horizon and LSS distribution. Both effects are sensitive to the composition.
2. A pure proton composition can be excluded, unless the dipole anisotropy is not due to LSS.
3. Both the Auger hot spot and the excess near the south galactic pole seen above 38 EeV can potentially be due to the large-scale distribution of matter, rather than individual dominant sources. An interesting future work, after a more accurate treatment of attenuation has been implemented, will be to quantitatively compare the quality of such a description to the starburst galaxy fit (Aab et al. 2018b).
4. The UHECR source scenarios with many lower-power sources rather than a few individual high-power sources or slow acceleration in large-scale accretion shocks remain competitive. The TA hot spot, currently at lower significance (Kawata et al. 2020), seems to require an individual source if it is real; this, and the constraints on the number density of sources, will be the topic of a separate report.
5. In the future, with higher fidelity in the attenuation modeling, the observed anisotropies from the known LSS should provide a powerful constraint on the GMF, finally overcoming the chicken-and-egg problem of needing to know the sources in order to use deflections to improve the GMF so that deflection predictions can be made more reliable as needed to identify the sources.

We thank Yehuda Hoffman for his permission to use the density field from Hoffman et al. (2018), Daniel Pomarède for the 3D visualization, Marco Muzio, Olivier Deligny, Denis Allard, and Anatoli Fedynitch for valuable discussions, Shenglong Wang for assistance with the use of the NYU high-performance computing facility, and members of the

Pierre Auger Collaboration for helpful comments on the manuscript. G.R.F. acknowledges membership in the Pierre Auger Collaboration. The research of N.G. was supported by New York University and the Simons Foundation, and that of G.R.F. was supported by NSF-1517319 and NSF-2013199. Some of the results in this Letter have been derived using the healpy (Zonca et al. 2019) and HEALPix (Gorski et al. 2005) packages.

Appendix A IM Calculation Procedure

To calculate the IM, (i) we assume that the 3D cosmic-ray source distribution follows the LSS, and (ii) we treat the UHECR diffusion in the EGMF by taking it to be homogeneous and characterized by a diffusion coefficient D_{EG} .

A.1. Source Distribution

We assume that the UHECR source density is proportional to the matter density field, $\rho(r, \hat{e})$, where r is the radial coordinate and \hat{e} is the direction in the sky. The density contrast is $\delta(r, \hat{e}) = 1 - \rho(r, \hat{e})/\bar{\rho}$, where $\bar{\rho}$ is the mean density of the universe. To model the matter density, we use the same set of simulations as in Globus et al. (2019b), i.e., cosmological simulations constrained by the CosmicFlows-2 data (Tully et al. 2013). Up to a distance of 350 Mpc, this uses the quasi-linear density field presented in Hoffman et al. (2018), for which the angular resolution of the boxes is 1.5–2 Mpc. (Note that this is larger than the extent of the 2MRS catalog, which is flux-limited and whose sampling falls off beyond ~ 100 Mpc.) Beyond 350 Mpc, the density field is obtained in the linear regime using a series of constrained realizations within a 1830 Mpc depth (see Globus et al. 2019b, for more details). Beyond 1830 Mpc, we simply assume that the universe is homogeneous. Therefore, thanks to the CosmicFlows-2 matter density field, we have the intensity sky maps of different shells of distances. In the “shell image,” the intensity of each pixel is proportional to the source density in that pixel, $I_0(r, \hat{e}') \equiv \delta(r, \hat{e}')$. The angular resolution of each shell image is 1° .

A.2. Single Source Image

The intensity profile of a cosmic-ray source depends on the scattering properties of the UHECRs in the EGMF. The diffusion coefficient, D_{EG} , can be approximated by a fitting function taking into account both the resonant and nonresonant diffusion regimes (Globus et al. 2008),

$$D_{\text{EG}} \approx 0.03 \left(\frac{\lambda_{\text{Mpc}}^2 E_{\text{EeV}}}{Z B_{\text{nG}}} \right)^{1/3} + 0.5 \left(\frac{E_{\text{EeV}}}{Z B_{\text{nG}} \lambda_{\text{Mpc}}^{0.5}} \right)^2 \text{Mpc}^2 \text{Myr}^{-1}, \quad (\text{A1})$$

where Z is the charge of the cosmic ray, E_{EeV} is its energy measured in EeV, B_{nG} is the EGMF strength in nG, and λ_{Mpc} is the EGMF coherence length λ_c in Mpc.

The single scattering angle depends on the optical depth, $\tau = rc/D_{\text{EG}}$, where r is the distance from the source. It is

characterized by the rms value

$$\langle \delta\theta^2 \rangle \sim (\lambda_c/r_L)^\kappa \langle \delta B^2/B^2 \rangle, \quad (\text{A2})$$

where r_L is the Larmor radius $r_L = 1.1 (\text{Mpc} E_{\text{EeV}} / (Z B_{\text{nG}}))$, and $\kappa = 2$ for $\lambda_c \leq r_L$ and $\kappa = -2/3$ for $\lambda_c > r_L$ for Kolmogorov turbulence (Kotera & Lemoine 2008). We assume strong turbulence ($\langle \delta B^2 \rangle / B^2 = 1$), so $\langle \delta\theta^2 \rangle \sim (\lambda_c/r_L)^\kappa$.

To estimate the single source image (e.g., intensity sky map), we follow the same formalism as the diffusion of light in scattering media, described by the radiative transfer theory (Chandrasekhar 1960). In the case of a spherically symmetric atmosphere, the radiative transport equation that describes the change in flux through an infinitesimal volume is given by

$$\mu \frac{\partial I}{\partial \tau} + \frac{1 - \mu^2}{\tau} \frac{\partial I}{\partial \mu} = -\frac{I(\tau, \mu)}{4\pi} \int_0^{2\pi} \int_{-1}^1 P(\cos \delta\theta) I(\tau, \mu') d\mu' d\phi', \quad (\text{A3})$$

where $P(\cos \delta\theta)$ is the phase function, and $\cos \delta\theta$ is the cosine of the angle between the incident direction (θ', ϕ') and the scattered one in the direction (θ, ϕ), $\mu = \cos \theta$ and $\mu' = \cos \theta'$ (see Figure A1 for clarity).

A general phase function that holds for inhomogeneities of various sizes is the Henyey & Greenstein (1941) phase function,

$$P(\cos \delta\theta) = \frac{1 - q^2}{(1 - 2q \cos \delta\theta + q^2)^{3/2}}, \quad (\text{A4})$$

where $q = \langle \cos \delta\theta \rangle$. In the context of cosmic-ray scattering on magnetic field inhomogeneities, $\delta\theta \sim (\lambda/r_L)^\kappa$ (see above). Therefore, we have two cases:

1. in the weak scattering regime, $\delta\theta \ll 1$ and $q \sim 1$ (small angle scattering), and
2. in the resonant scattering regime, $\delta\theta \sim 1$ and $q \sim 0$ (large angle scattering).

The intensity of a single source in the sky can be calculated using Equations (A3)–(A4),

$$I(\tau, \mu) = \sum_{m=0}^{\infty} (g_m(\tau) + g_{m+1}(\tau)) L_m(\mu), \quad (\text{A5})$$

where $I(\tau, \mu)$ is the intensity of an isotropic point source for a given radial direction θ , $L_m(\mu)$ is the Legendre polynomial of order m , $g_m(\tau) = I_0 \exp(-\beta_m \tau - \alpha_m \log \tau)$, $\beta_m = (2m+1)/m(1-q^{m-1})$, $\alpha_m = m+1$, and $g_0(\tau) = 0$ (see Narasimhan & Nayar 2003, for more details). The number of coefficients used in our calculations is $m = 300$. The resulting $I(\tau, \mu)$ corresponds to the point-spread function (PSF) that describes the response of the EGMF to a point source (see examples in Figure A2). We use this PSF to calculate the observed intensity map for each shell of distance after diffusion in the EGMF $I_R(r, \hat{e})$,

$$I_R(r, \hat{e}) = I_0(r, \hat{e}') * \text{PSF}(r, D_{\text{EG}}, \delta\theta), \quad (\text{A6})$$

where the asterisk is the convolution operator and $I_0(r, \hat{e}')$ is the original “shell image” at a distance r .

Finally, the “illumination map,” $I_j(\hat{e}, D_{\text{EG}})(E)$, the map of the total UHECR flux illuminating the Galaxy for a composition j at energy E , is obtained by summing the intensity sky map for each shell (Equation (A6)), with the weighting determined by energy losses and composition evolution.

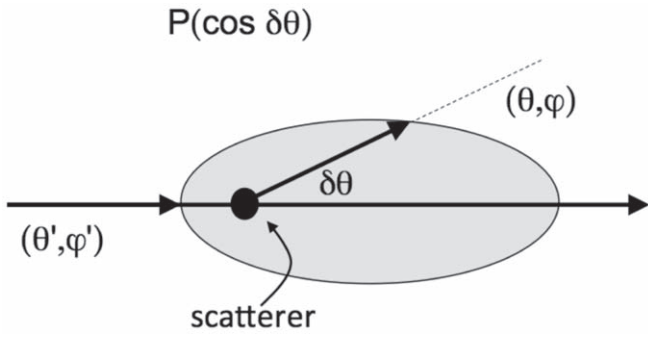


Figure A1. Definition of the different quantities used in the calculations and the single scattering angle $\cos \delta\theta$. The gray shaded area illustrates the phase function $P(\cos \delta\theta)$ (Equation (A4)) introduced by Henyey & Greenstein (1941), which, by the variation of one parameter q , ranges from backscattering through isotropic scattering to forward scattering. Note that for cosmic rays, there is only isotropic (resonant scattering) and forward scattering (weak scattering).

A.3. UHECR Horizon

In this work, we have employed two methods of weighting the shells. The first method is that used by Globus et al. (2019b), in which all shells up to a maximum distance (which they designated the UHECR horizon, $H_j(E)$) are given equal weight, and shells at larger distances make zero contribution. An improvement on this “sharp cutoff” treatment, short of a full analysis, is the “exponential attenuation” of Equation (1) discussed in Section 2.2.

“Sharp cutoff” treatment. The following is the treatment of Globus et al. (2019b). With no EGMF, the UHECR horizon is taken to be the mean total energy loss length, $\chi_{\text{loss}} = -c(d \ln E/dt)^{-1}$, including the contribution of pair production and photodisintegration processes (e.g., see Allard et al. 2006, for more details about the calculations). The energy loss length is calculated using the giant dipole resonance cross sections discussed in Khan et al. (2005) and, for the higher-energy processes (pion production), the parameterization of Rachen (1996).

For a nucleus j with energy E , denote

$$H_j(E) \approx \min(\sqrt{d_{\text{diff}} d_{\text{GZK}}}, d_{\text{GZK}}), \quad (\text{A7})$$

where d_{GZK} is taken to be the energy attenuation length, χ_{loss} , the distance within which a cosmic ray loses $\sim 63\%$ of its initial energy (Globus et al. 2019b), and $d_{\text{diff}} \sim 6D_{\text{EG}}/c$ (Globus et al. 2008) is the rigidity-dependent diffusion distance. For the rigidity range considered, the propagation of cosmic rays is almost ballistic (i.e., the diffusion coefficient is given by the

right-hand side of Equation (A1)), so the path length of the UHECR is approximately the rectilinear distance to the source (see also Globus et al. 2008, for more details). Figure A3 shows the horizon $H_j(E)$ from Equation (A7) for the best-fit parameters. We calculate illumination sky maps, $I_j(\hat{e}, D_{\text{EG}})(E)$, for different compositions j ($Z = 1, 2, 6, 8, 14, 26$) and diffusion coefficients D_{EG} in 25 rigidity bins.

The “exponential attenuation” treatment. Our second approach to attenuation, the “exponential attenuation” treatment, weights the shells by Equation (1), where $d_{90}(A, E)$ is the distance within which 90% of the parents of an observed cosmic ray of (A, E) originated. We take $d_{90}(A, E)$ from Globus et al. (2008), which adopted a spectral index of -2.4 and mixed composition at the source, as in Allard et al. (2005). Figure A4 shows that the 2005 High Resolution Fly’s Eye (HiRes) spectrum used by Globus et al. (2008) is similar to the most up-to-date Auger spectrum (Aab et al. 2020b, 2020c) imposed in our analysis.

The Auger collaboration (Aab et al. 2017b) performed a combined fit to spectrum and composition and found that the best-fitting spectral index depends on the HIM used to interpret the X_{max} data, as well as the extragalactic background light and photointeraction models used. With EPOS-LHC, they found a production spectral index ≈ -1 , while other models are compatible with a softer index around -2 . It would be desirable to test the sensitivity of our results to the d_{90} modeling by using $d_{90}(A, E)$ tables for the combined fit to the spectrum and composition at the source performed by Aab et al. (2017b), but these are not available in the literature. We remark that a bias from using integrated rather than binned $d_{90}(A, E)$ tends to offset that of using a too-soft production spectral index in generating the $d_{90}(A, E)$ tables. If the spectrum is actually harder than -2.4 , the true $d_{90}(A, E)$ values will be smaller than adopted, while $d_{90}(A, E)$ for events integrated over the spectrum above E is smaller than $d_{90}(A, \lg E)$ for the single $\lg E$ energy bin at E because the horizon decreases with energy. Thus, our procedure using the Globus et al. (2008) d_{90} tables, which may use a too-soft spectral index, should be relatively insensitive to the spectral index assumption. Since the d_{90} approach is inherently inadequate in any case, we have chosen not to invest energy in producing alternate tables ourselves, as would be needed to explore the sensitivity to the assumed source spectrum and composition embedded in the $d_{90}(A, E)$ s used. A complete, correct treatment must self-consistently model the spectrum and composition at the source and treat the attenuation of nuclei as motion in $\{A, E\}$ space during propagation.

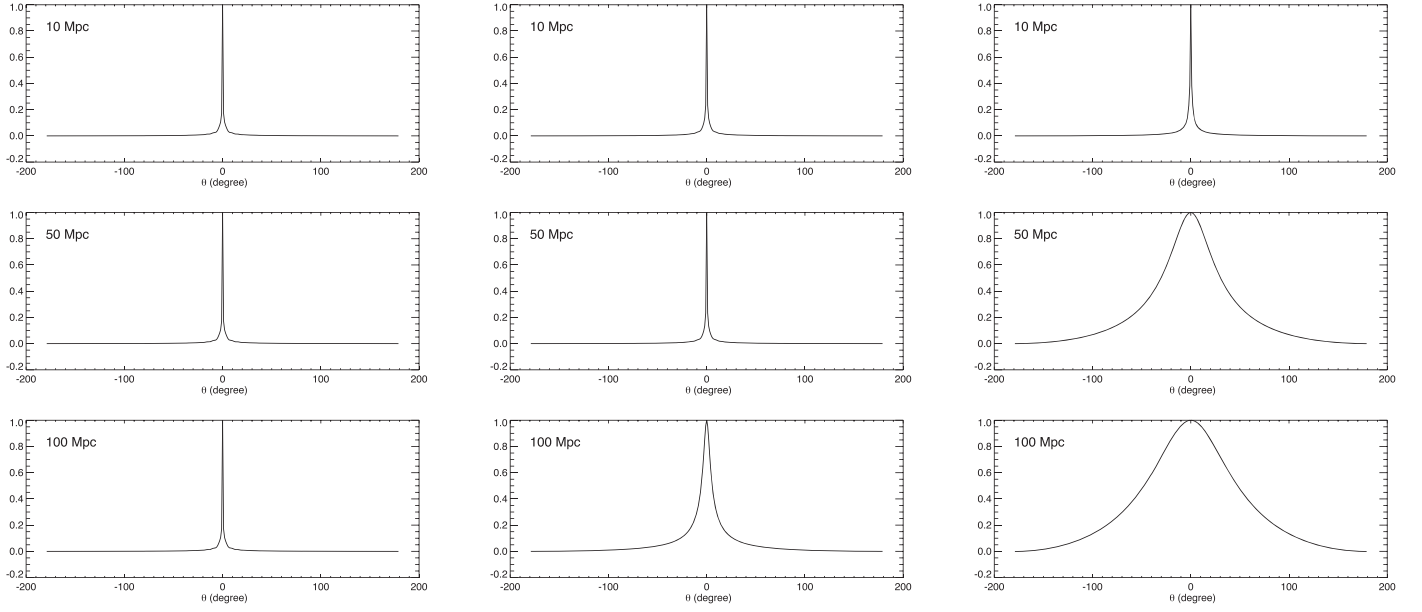


Figure A2. The PSF (Equation (A5)) of a single source as a function of distance for (left to right) 0.3, 0.5, and 1 nG for nitrogen ($Z = 7$) at 11.5 EeV (this is the median value of the energy bin ≥ 8 EeV), i.e., a rigidity of ~ 1.6 EV. One can see that for our best-fit parameter model (~ 0.3 nG), the spreading due to the EGMF is negligible.

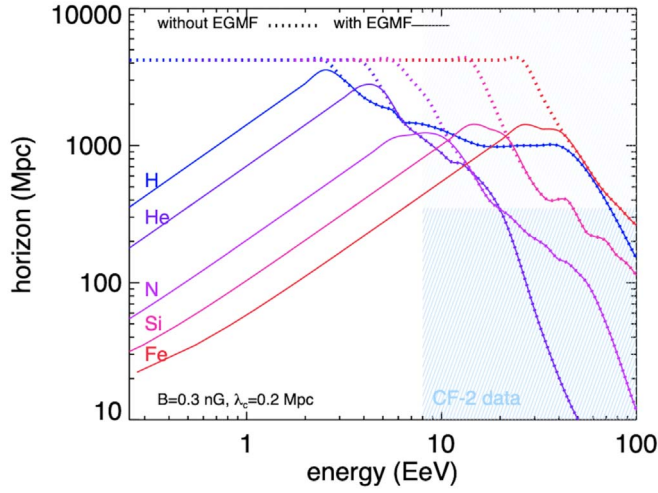


Figure A3. The UHECR horizon (energy loss length) as a function of energy for the best-fit parameters of the SH* case, $B_{EG} \sim 0.3$ nG and $\lambda_{EG} = 0.2$ Mpc, for five different nuclei j : H, He, N, Si, and Fe. The extent of the CosmicFlow-2 reconstruction of the local universe is figured by the blue shaded area. For comparison, the case of zero EGMF is also shown.

Appendix B Arrival Map Calculation Procedure

B.1. Arrival Map Calculation Procedure

Once the IM is known, one can build the arrival map using the calculation of cosmic-ray trajectories in the GMF model of JF12. Farrar & Sutherland (2019) provided nearly two billion simulated backtracking trajectories for GMF coherence lengths $\lambda_{\text{coh}} = 30$ and 100 pc, with RK4 precision of 10^{-8} . In order to have more choices of λ_G , we mix the trajectories of 30 and 100 pc with different weights to interpolate between them.

We pixelate the sky map with HEALPix pixels, as they are equal-area pixelation of the sphere. We use HEALPix resolution 5, such that there are 12,288 pixels in the sky. The mean spacing of the pixels is $1^\circ 8323$, which is fine enough for

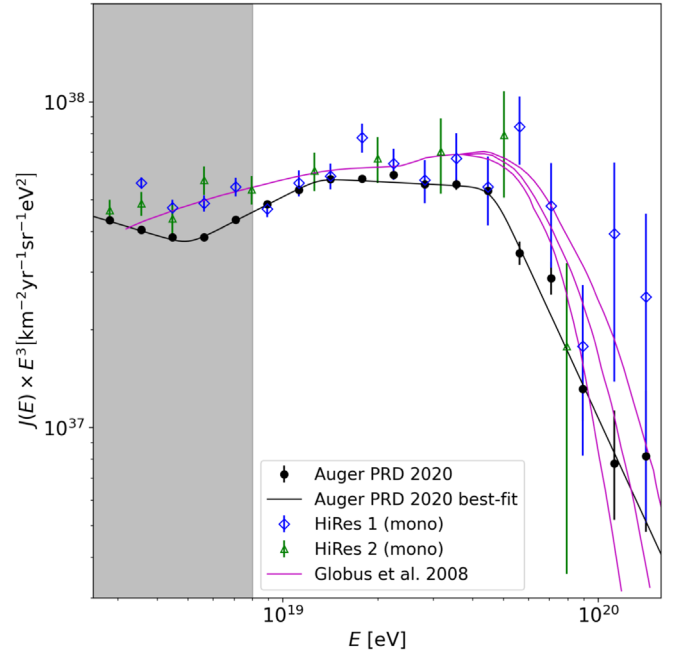


Figure A4. Most up-to-date UHECR spectrum from the Pierre Auger Observatory (Aab et al. 2020b, 2020c; black dots) with the Auger multi-power-law best fit shown by the black line. We take the Auger fit of the energy spectrum as an input to the model. The blue and green markers show the measurement by HiRes (Abbasi et al. 2005), with the pink lines being the model of Globus et al. (2008) that was guided by the HiRes data and the source of our $d_{90}(A, E)$ values, showing generally good agreement apart from a small offset that is consistent with energy-scale uncertainties. The region of the plot below 8 EeV is shaded because it is not relevant to this Letter.

modeling purposes. Each “source arrival matrix” M_{hi}^{kn} (described below) is about 1.2 GB in file size, which is suitable for the memory space allowed by high-speed computation.

Below is the exact procedure of calculating the model arrival map from the IM. Start with the following notations.

1. The model parameter labels $\{m, n, q\}$ label which value of D_{EG} , λ_c , and composition parameter Ω is being discussed.
2. The S_h denotes the IM, i.e., the cosmic-ray flux illuminating the surface of the Milky Way in HEALPix direction h .
3. The A_i denotes the arrival map, i.e., the cosmic-ray flux arriving at Earth in HEALPix direction i .
4. The M_{hi}^{kn} denotes the source arrival matrix that contains information about deflection of cosmic rays in the GMF. The matrix elements are the numbers of trajectories from source direction h to arrival direction i for rigidity k and GMF coherence length n .
5. The V_{jk}^{lq} denotes the rigidity spectrum, i.e., the abundance of cosmic rays $\frac{dN}{d \lg R}$ of chemical element j , rigidity bin k , and energy threshold l for composition parameter q . It is derived from the energy spectrum and composition parameter, as discussed in Section D.1.
6. The m denotes the EGMF diffusion coefficient.
7. The ω_i denotes the directional exposure of the Pierre Auger Observatory in HEALPix direction i .

The arrival map of each cosmic-ray species in each rigidity bin can be calculated from the IM and source arrival matrix by

$$A_i^{jkmn} = \sum_h S_h^{jkm} M_{hi}^{kn}. \quad (\text{B1})$$

By combining the individual arrival maps with weights given by the rigidity spectrum, the arrival map of all cosmic rays in energy bin l with parameter set mnq is

$$\mathcal{A}_i^{lmnq} = \sum_{jk} A_i^{jkmn} \frac{V_{jk}^{lq}}{\sum_i \omega_i A_i^{jkmn}}. \quad (\text{B2})$$

The ω_i is included in the denominator to ensure that one would obtain an energy spectrum exactly as observed by Auger with partial exposure, in case the full-sky spectrum is slightly different from the spectrum observed by Auger with partial exposure.

Finally, the IM of all cosmic rays is

$$S_h^{lmnq} = \sum_{jk} S_h^{jkmn} \frac{V_{jk}^{lq}}{\sum_i \omega_i A_i^{jkmn}}. \quad (\text{B3})$$

B.2. Reconstructing the Dipole Component from the Sky Map with Partial Exposure

There are two prominent ways to reconstruct a dipole from an observed data set with partial exposure: the Rayleigh analysis and the K-inverse method. We tested both in earlier works (Globus et al. 2019a). The two methods give similar results. The differences between the Rayleigh analysis and K-inverse method are mainly manifested in d_z . This is expected because the directional exposure is zero for decl. above 45° , and it is difficult to measure d_z with such incomplete coverage. For the Auger data set, the Rayleigh analysis is preferred because it is less sensitive to the systematics of the experiment. However, since we are working from a full-sky model, it is most straightforward to use the K-inverse method to reconstruct the dipole that would be inferred using the Rayleigh method, given Auger's limited exposure. Table E2 gives the dipole components of both the full-sky model arrival map and

the dipole components reconstructed from the model arrival map weighted with Auger's exposure.

B.3. Top-hat Smoothing Procedure

To smooth the flux map with a 45° top-hat function for plotting, a standard procedure, used in Aab et al. (2018a), consists of dividing the number of events in a region (45° radius disk excluding the zero-exposure region) by the total exposure in that region. An alternative way consists of weighting each event by the inverse exposure for its arrival direction, summing the weight of events in the region, and dividing by the solid angle of the region (45° disk excluding zero-exposure region) as in Deligny (2016). We use this alternative way, which leads to some differences. In particular, the excess in the region $180^\circ < l < 210^\circ$ and $30^\circ < b < 60^\circ$ appearing in the Auger top-hat map ≥ 32 EeV (Aab et al. 2018a) may be an artifact, as it does not appear in the sky map created using the Deligny (2016) smoothing method applied to our backed-out events above 38 EeV, nor is such an excess present in the LSS model map in Figure 4.

Appendix C

The Effect and Uncertainty of the JF12 GMF Model

In this section, we discuss the JF12 model uncertainties. The UHECRs from a given direction receive a net deflection from the ordered component of the field, as well as being spread out by the turbulent component. Besides deflecting and diffusing the arrival directions of cosmic rays, the GMF can amplify or reduce the flux at Earth, depending on the direction of cosmic rays entering the Galaxy and their rigidity. This effect is naturally incorporated in the Farrar & Sutherland (2019) trajectories.

Being more general and constrained by more data, JF12 is the generally adopted model of the coherent GMF. A strong point of JF12 relative to other GMF models is that JF12 used polarized synchrotron emission and not just RMs for constraining the model parameters, thus constraining the transverse as well as line-of-sight components of the magnetic field. However interpreting the all-sky RM, Q , and U measurements requires 3D models of the thermal and cosmic-ray electron distributions, and the models available in 2012 (and still now) are rather primitive, limiting the accuracy of the inferred coherent GMF. The JF12 random field model was based on unpolarized synchrotron emission maps from WMAP. Since then, Planck has found the unpolarized synchrotron emission to be considerably less than WMAP reported (Planck Collaboration et al. 2016) due to a different treatment of other contributions. This could potentially lead to a substantial reduction in the magnitude of the random component of the GMF. (For further discussion, see Farrar 2014 and Planck Collaboration et al. 2016.) While we do not have trajectories simulated in a weaker random field, functionally speaking, the $\lambda_c = 30$ pc simulations of Farrar & Sutherland (2019) have a similar qualitative effect to a reduced field strength.

Appendix D

Fitting Methodology

D.1. Composition Modeling and Likelihood

The mass composition of cosmic rays can be inferred from measurements of the maximum atmospheric depth of air

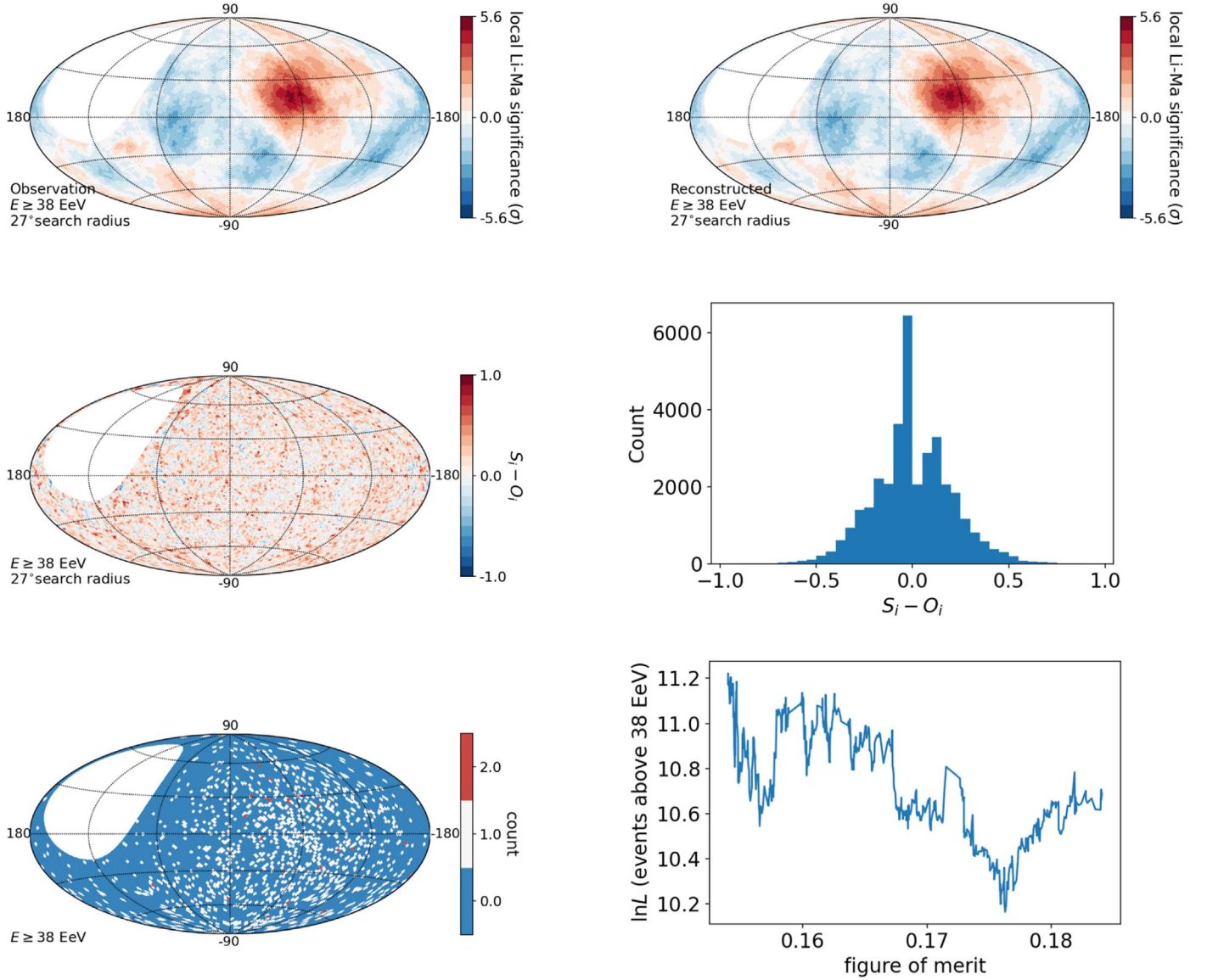


Figure D1. Upper plots: Li–Ma significance sky map from Caccianiga (2019) (left) and that calculated from reconstructed arrival directions (right). Middle: sky map (left) and histogram (right) of $S_i - O_i$, i.e., the difference in the Li–Ma sky map between observation and reconstruction. Lower right: evolution of the value of Equation (D8) for the model case SH* as the figure of merit is minimized. The variation is relatively small compared to its value. A larger $\ln L$ means the model better fits the arrival directions of events above 38 EeV.

showers, X_{\max} , by the Auger collaboration (Yushkov 2019). The mean and variance of $\ln A$ (A is the mass number) and their uncertainties at eight energy levels are inferred using three different HIMs: Sibyll2.3 c, EPOS-LHC, and QGSJETII-04.

Even though we are informed by X_{\max} measurements, given the uncertainty on the composition from the HIMs, we parameterize the evolution of the composition with energy and take the X_{\max} -derived composition as constraints along with the dipole anisotropy. We parameterize the composition as follows (abbreviating $\log_{10}(E) \equiv \lg E$):

1. $\langle \ln A \rangle = \alpha \lg E + \langle \ln A \rangle_{8\text{EeV}}$ and
2. $\sigma^2(\ln A) = \beta \lg E + \sigma^2(\ln A)_{8\text{EeV}}$.

Thus, the model composition is characterized by four parameters: $\Omega \equiv \{\alpha, \beta, \langle \ln A \rangle_{8\text{EeV}}, \sigma^2(\ln A)_{8\text{EeV}}\}$.

The following discussion is about how to calculate $\ln L(\langle \ln A \rangle | \Omega; \text{HIM}) + \ln L(\sigma^2(\ln A) | \Omega; \text{HIM})$, i.e., the log of likelihood that the true mean and variance of $\ln A$ at eight

energy levels are indicated by Ω , given that a particular HIM is true.

Let us use the following notations.

1. The N is the total number of energy bins of X_{\max} measurement relevant to this study; in this case, $N = 8$. The $\langle \lg E \rangle$ are 18.95, 19.05, 19.15, 19.25, 19.35, 19.44, 19.55, and 19.73.
2. The $\Omega_1 \equiv \{\alpha, \langle \ln A \rangle_{8\text{EeV}}\}$ is the set of two parameters regarding $\langle \ln A \rangle$.
3. The \mathbf{x} is the $\langle \ln A \rangle$ of cosmic rays in N energy bins inferred by a chosen HIM.
4. The \mathbf{m} is the $\langle \ln A \rangle$ of cosmic rays in N energy bins specified by Ω_1 .
5. The s is the systematic uncertainty of \mathbf{x} in N energy bins of the chosen HIM.
6. The σ is the statistical uncertainty of \mathbf{x} in N energy bins of the chosen HIM.
7. The \mathbf{C} is the covariance matrix $C_{ij} = \sigma_i^2 \delta_{ij} + s_i s_j$.

For each HIM and parameter set Ω_1 ,

$$L(\langle \ln A \rangle | \Omega; \text{HIM}) \equiv p(\mathbf{x} | \mathbf{m}) = B \exp(-\chi_{\min}^2 / 2), \quad (\text{D1})$$

$$\chi_{\min}^2 = (\mathbf{x} - \mathbf{m})^T \mathbf{C}^{-1} (\mathbf{x} - \mathbf{m}), \quad (\text{D2})$$

$$B = [(2\pi)^N \det \mathbf{C}]^{-1/2}, \quad (\text{D3})$$

$$\ln L = -\frac{1}{2} [(\mathbf{x} - \mathbf{m})^T \mathbf{C}^{-1} (\mathbf{x} - \mathbf{m}) + \ln(\det \mathbf{C}) + N \ln(2\pi)]. \quad (\text{D4})$$

The lower and upper systematic uncertainty of $\langle \ln A \rangle$ are not equal, such that s and \mathbf{C} are not uniquely defined. So we introduce a nuisance parameter η such that the systematic shift of x_i is ηs_i . With either an upper or a lower systematic uncertainty, one can calculate

$$\chi_{\min}^2 = \min_{\eta} \left(\sum_{i=1}^N \frac{(m_i - x_i - \eta s_i)^2}{\sigma_i^2} + \eta^2 \right) \quad (\text{D5})$$

and compare the two χ_{\min}^2 to determine if the lower or upper systematic uncertainty should be applied. Then \mathbf{C} is uniquely defined, and one can proceed to calculate $\ln L$ using Equation (D11).

The calculation procedure of $\ln L(\sigma^2(\ln A) | \Omega; \text{HIM})$ is similar to that of $\ln L(\langle \ln A \rangle | \Omega; \text{HIM})$. The only difference is that the lower and upper statistical uncertainties of $\sigma^2(\ln A)$ are not equal either. The calculation takes more effort, but the concept is clear. First, use Equation (D5) to determine if the upper/lower systematic uncertainty should be used for all x_i and the upper/lower statistical uncertainty should be used for individual x_i ; then determine \mathbf{C} and calculate $\ln L$ using Equation (D11).

We consider seven chemical elements, p, He, C, O, Ne, Si, and Fe, and mix them such that the $\langle \ln A \rangle$ and $\sigma^2(\ln A)$ in each narrow $\lg E$ bin of width 0.02 are as specified by a given choice of Ω . The fractions are in general not unique, but if we use fewer composition bins unphysical discretization effects would be introduced. To choose among the different solutions, we adopt the one whose element fractions have the median skewness of $\langle \ln A \rangle$. In the case that certain $\sigma^2(\ln A)$ cannot be achieved, we take the element fractions that give the closest value. We tested this procedure using the all-A composition predictions of the Muzio et al. (2019) model. In order to compare with the Auger data of $\langle \ln A \rangle$ and $\sigma^2(\ln A)$ that use wider energy bins, we group narrow energy bins together accordingly.

D.2. Likelihood of Dipole Components

The Auger measurement of dipole components d_x , d_y , d_z of three energy bins of 8–16, 16–32, and ≥ 32 EeV are independent of one another (Aab et al. 2018a). The formula below is used to calculate the log-likelihood for Auger to measure the dipole component d_i with value x_i and Gaussian uncertainty σ_i if the true dipole component m_i is given by the model:

$$\ln L(\text{dipole} | \Theta; \text{source}) = \sum_{i=1}^9 \ln \left[\frac{1}{\sqrt{2\pi} \sigma_i} \exp\left(-\frac{(x_i - m_i)^2}{2\sigma_i^2}\right) \right]. \quad (\text{D6})$$

D.3. Likelihood of Arrival Directions of Events above 38 EeV

To check the compatibility of our LSS model with the observations, we performed a hypothesis test using the same test statistic as in Aab et al. (2018b) and Abbasi et al. (2018) based on the log-likelihood ratio. With an isotropic flux model $\Phi_{\text{ISO}}(\hat{n})$ and a model flux model $\Phi_{\text{model}}(\hat{n})$ as null hypothesis and alternative hypothesis, respectively, the test statistic is defined as twice the log-likelihood ratio,

$$\text{TS} = 2 \ln(L(\Phi_{\text{model}}) / L(\Phi_{\text{ISO}}))$$

$$\text{where } L(\Phi) = \prod_i \frac{\Phi(\hat{n}_i) \omega(\hat{n}_i)}{\int_{4\pi} \Phi(\hat{n}) \omega(\hat{n}) d\Omega}, \quad (\text{D7})$$

with \hat{n}_i being the arrival direction of the i th observed event and $\omega(\hat{n})$ being the directional exposure of the Auger experiment. We define

$$\ln L(\text{events} | \Theta; \text{source}) \equiv \ln(L(\Phi_{\text{model}}) / L(\Phi_{\text{ISO}})) = 0.5 \text{ TS}. \quad (\text{D8})$$

This way, it is the correct log-likelihood that can be added with the log-likelihood from other aspects (such as composition), and it is normalized such that $\ln L(\text{events} | \Theta; \text{source}) = 0$ if ISO is the model.

D.4. Reconstructing the Arrival Directions of Events above 38 EeV

The arrival directions of events above 38 EeV used for the Caccianiga (2019) analysis are not yet published, but they are needed because Equation (D8) is the best way to measure the similarity between the model and data. We digitized the Li–Ma significance sky map in Figure 1 of Caccianiga (2019) and used it to reconstruct the arrival directions of the events. The reconstruction procedure is as follows. We uniformly tiled the sky with 12,288 HEALPix pixels of area 3.357 deg², so each 27° circle consists of a batch of 682 pixels. Let us use the following notations.

1. The N_{tot} is the total number of events above 38 EeV; $N_{\text{tot}} = 1288$.
2. The n_{pix} is the total number of HEALPix pixels that have nonzero detector exposure; $n_{\text{pix}} = 10,477$.
3. The n_{grid} is the total number of data points in the Auger Li–Ma sky map. The data is in a 1° grid in equatorial coordinates (R.A. and decl.) excluding the zero-exposure region.
4. The \mathbf{N} is a 1D array of length n_{pix} that represents the number of events in each individual pixel, with the sum of all elements being N_{tot} .
5. The \mathbf{N}_{on} is a 1D array of length n_{grid} that represents the number of events inside each 27° circle centered at each grid point.
6. The $\boldsymbol{\alpha}$ is a 1D array of length n_{grid} that represents the probability of an event falling inside each 27° circle if the flux is isotropic; it is effectively the exposure in each circle divided by total exposure.
7. The \mathbf{A} is a 2D matrix comprised of ones and zeros such that A_{ij} represents whether pixel j belongs to the batch of pixels that represent the circle centered at grid point i ; the matrix is n_{grid} by n_{pix} .

8. The \mathbf{S} is a 1D array of length n_{grid} that represents the Li–Ma significance of a trial data set at each grid point.
9. The \mathbf{O} is a 1D array of length n_{grid} that represents the Li–Ma significance of the observation data at each grid point.
10. The f is the function of Li–Ma significance as in Equation (17) of Li & Ma (1983).

The following relationships hold:

$$AN = N_{\text{on}} \quad (\text{D9})$$

and

$$S = f(N_{\text{on}}, N_{\text{tot}}, \alpha). \quad (\text{D10})$$

We turned the reconstruction of arrival directions into a computation problem. Moving an event from one pixel to another effectively alters N and subsequently alters N_{on} and S . The goal is to find the best N that minimizes the discrepancy between \mathbf{S} and \mathbf{O} . We set the objective function for minimization as

$$\text{figure of merit} = \frac{1}{n_{\text{grid}}} \sum_i^{n_{\text{grid}}} |S_i - O_i|. \quad (\text{D11})$$

We started with a random set of arrival directions. Then we calculated how much improvement could be made to the figure of merit if any one event was moved from one pixel to another. A movement was accepted if it improved the figure of merit. We kept moving individual events one at a time until no further improvement could be made. The figure of merit reached 0.162, which was a local minimum. In order to further improve the reconstruction, we had to let it get out of the local minimum by moving multiple events at once. We randomly selected six events within an angular distance of 54° , and each event was allowed to move to any of its four neighboring pixels or stay

where it was. We repeated this procedure until the figure of merit reached 0.154. We believed this was sufficiently good for our purpose, and we did not spend more computation resources on it. The upper two plots of Figure D1 show the Li–Ma significance sky map from Caccianiga (2019) and that from reconstruction. They look very alike. The middle two plots show the sky map and histogram of $S_i - O_i$. One can see that the excesses and deficits of $S_i - O_i$ are randomly distributed in the sky map. The lower left plot shows the reconstructed arrival directions in a sky map. The lower right plot shows the evolution of the value of Equation (D8) with the best-fit (fixed) parameters of case SH* as the figure of merit is minimized. The variation in the value of Equation (D8) is sufficiently small that it does not affect the results of this Letter. Comparing the arrival directions in the best reconstruction with those in previous iterations, the arrival directions of many cosmic rays have not been changed, and those of the rest of the cosmic rays are moved by 1 or 2 pixels. The mean spacing of pixels is $1^\circ 83'$, so we estimate that the accuracy of the reconstructed arrival directions is a few degrees. Apart from accuracy, the precision level of the reconstruction is limited by the pixelization of the sky. Having more pixels would increase precision but increase computation cost.

Appendix E More Result Details

E.1. Contribution from Individual Shells

The left columns of Figures E1–E4 show the IMs (UHECR flux illuminating the Galaxy) with unit weight from each shell in the SH*, d90, d90sp, and PP model cases. The middle and right columns show the arrival maps (after propagation in the JF12 GMF model) in energy bins ≥ 8 and ≥ 32 EeV for

Table E1
Summary of Model Parameters and Results for Cases in Addition to Those in Table 1

Cases		Iso	SH*	SH _E *	SH _Q *	SH _{forceQ} *	SH (Better Hot Spot)*
Model	Source model	Isotropic	LSS	LSS	LSS	LSS	LSS
	Distance weighting	...	Sharp	Sharp	Sharp	Sharp	Sharp
	HIM	Sibyll2.3 c	Sibyll2.3 c	EPOS-LHC	QGSJET	QGSJET	Sibyll2.3 c
Likelihood	$\ln L(\text{dipole} \Theta; \text{source})$	−3.4	14.5	13.8	13.9	−17.9	13.9
	$\ln L(\text{events} \Theta; \text{source})$	0 (Ref)	11.1	10.9	11.0	−11.3	9.6
	$\ln L(\langle \ln A \rangle \Omega; \text{HIM})$	4.4	4.0	3.8	−1.4	3.9	3.7
	$\ln L(\sigma^2(\ln A) \Omega; \text{HIM})$	−2.8	−3.3	−3.7	−8.0	−8.9	−3.3
	Sum of $\ln L$ (Equation (2))	−1.9	26.3	24.7	15.4	−34.2	23.8
Best-fit parameters	$\lg D_{\text{EG},5\text{EV}}$...	$2.79^{+0.60}_{-0.20}$	$2.79^{+0.60}_{-0.20}$	$2.79^{+0.60}_{-0.20}$	2.19	2.79
	$\lg \lambda_G$...	$1.58^{+0.10}_{-0.08}$	$1.58^{+0.13}_{-0.08}$	$1.61^{+0.08}_{-0.10}$	2.00	1.53
	$\langle \ln A \rangle_{8-10 \text{ EeV}}$	2.02	$1.76^{+0.19}_{-0.15}$	$1.64^{+0.18}_{-0.16}$	$1.62^{+0.15}_{-0.14}$	0.72	1.65
	$\langle \ln A \rangle_{\geq 40 \text{ EeV}}$	3.19	$2.87^{+0.17}_{-0.10}$	$2.84^{+0.13}_{-0.08}$	$2.77^{+0.08}_{-0.07}$	1.89	2.68
	$\sigma^2(\ln A)_{8-10 \text{ EeV}}$	0.31	$0.48^{+0.27}_{-0.20}$	$0.47^{+0.27}_{-0.24}$	$0.38^{+0.28}_{-0.18}$	0.49	0.57
	$\sigma^2(\ln A)_{\geq 40 \text{ EeV}}$	0.19	$0.09^{+0.32}_{-0.05}$	$0.09^{+0.34}_{-0.05}$	$0.05^{+0.13}_{-0.01}$	0.30	0.04
	B_{EG} if $\lambda_{\text{EG}} = 0.2 \text{ Mpc}$...	$0.32^{+0.08}_{-0.16}$	$0.32^{+0.08}_{-0.16}$	$0.32^{+0.08}_{-0.16}$	0.63	0.32
Hot spot	Number of events in 27° circle centered at (309°7, 17°4). Obs = 188	125^{+11}_{-11}	154^{+12}_{-11}	156^{+12}_{-12}	160^{+12}_{-11}	155^{+12}_{-12}	168^{+12}_{-12}
	Li–Ma significance in 27° circle centered at (309°7, 17°4). Obs = 5.6	$0.0^{+1.0}_{-1.0}$	$2.7^{+1.1}_{-1.0}$	$2.8^{+1.1}_{-1.1}$	$3.2^{+1.0}_{-1.0}$	$2.7^{+1.1}_{-1.1}$	$3.9^{+1.0}_{-1.0}$

Note. For cases with asterisks (e.g., SH*), Equation (2) is maximized; i.e., models are fit to the composition, dipole, and events above 38 EeV. The best-fit parameters are reported as the median with 1σ confidence levels (i.e., 16th and 84th percentiles). In the last two rows, the hot-spot results are calculated from millions of mock data sets generated from the model arrival map above 40 EeV with the best-fit parameters. The confidence level represents the statistical uncertainty in the mock data data sets and does not represent the uncertainty due to the uncertainty in the best-fit parameters.

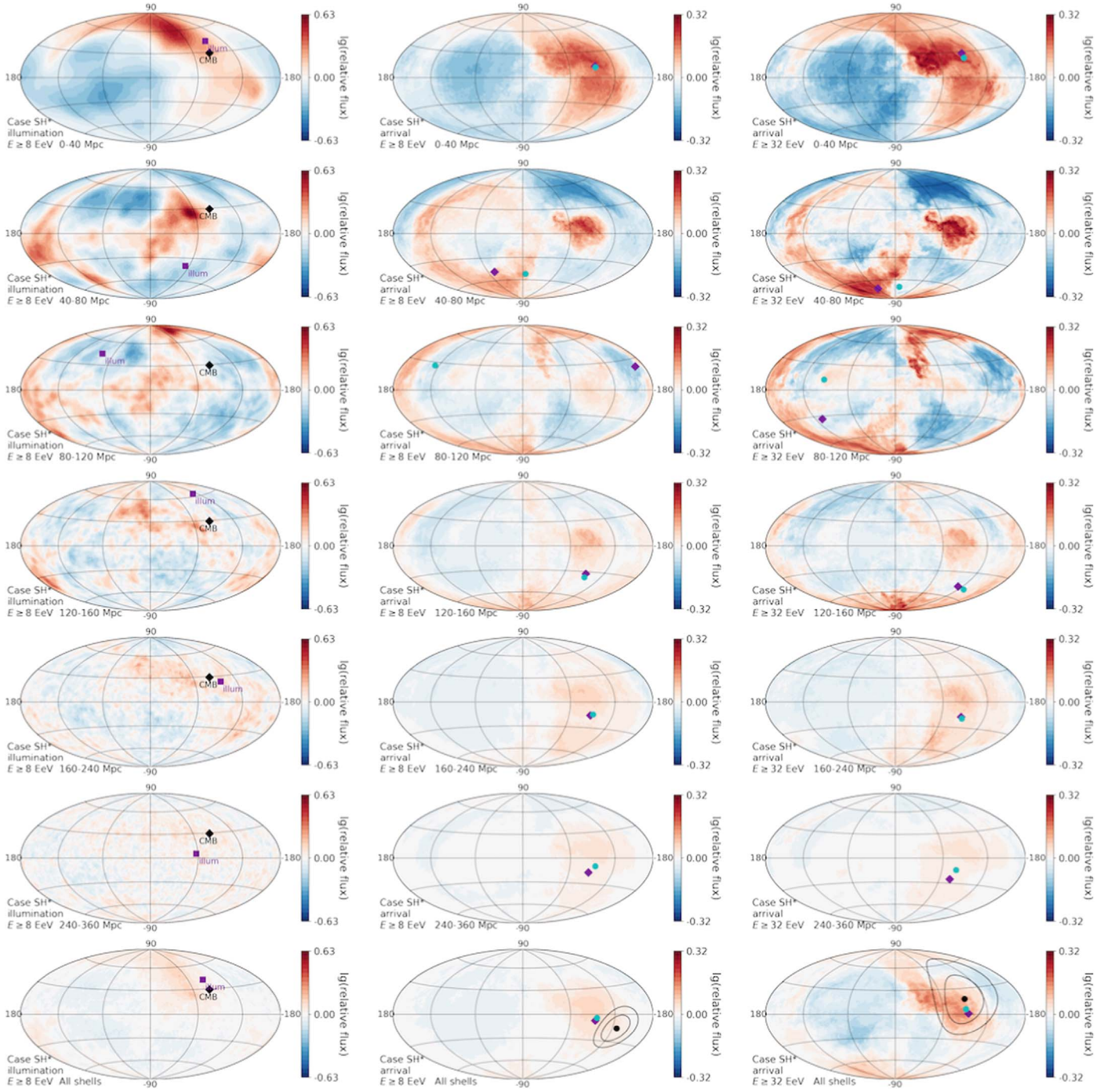


Figure E1. IMs (UHECR flux illuminating the Galaxy) and arrival maps (after propagation in the *JF12* GMF model) for the model case SH* and energy bins ≥ 8 and ≥ 32 EeV for different shells of distances.

Table E2
Comparison of Dipole and Quadrupolar Components ≥ 8 EeV between Observation and Model

Observable	Auger $l_{\max} = 1$	Auger $l_{\max} = 2$	Auger and TA All Multipoles	Case SH* $l_{\max} = 1$	Case SH* All Multipoles	Case d90 $l_{\max} = 1$	Case d90 All Multipoles
d_x	-0.008 ± 0.009	-0.004 ± 0.012	-0.007 ± 0.011	-0.032	-0.024	-0.024	-0.017
d_y	0.059 ± 0.009	0.054 ± 0.012	0.042 ± 0.011	0.039	0.031	0.026	0.022
d_z	-0.028 ± 0.014	-0.011 ± 0.035	-0.026 ± 0.019	-0.054	-0.048	-0.053	-0.042
Q		0.032 ± 0.014			0.025		0.020

Note. Since the Auger observatory has partial exposure coverage, the reconstruction of these components needs the assumption that the anisotropy is purely dipolar ($l_{\max} = 1$) or dipolar and quadrupolar ($l_{\max} = 2$). The joint result of Auger+TA in the last column has full-sky exposure coverage (di Matteo et al. 2020).

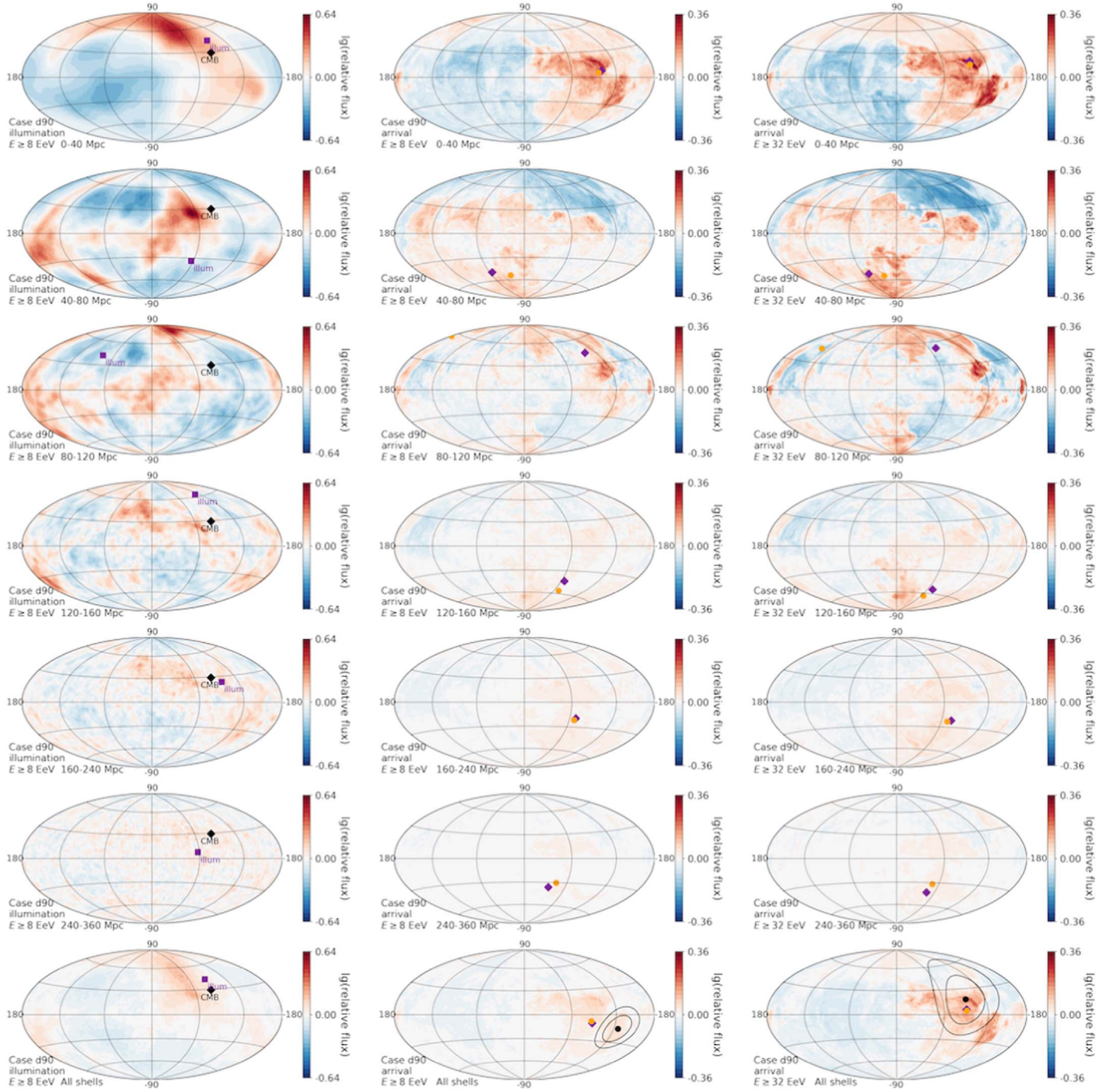


Figure E2. IMs (UHECR flux illuminating the Galaxy) and arrival maps (after propagation in the JF12 GMF model) for the model case d90 and energy bins ≥ 8 and ≥ 32 EeV for different shells of distances.

different shells of distances. The maps in the last row include cosmic rays from all distances with attenuation treatment.

The d90sp model uses the composition of the best-fitting SH* model with the exponential attenuation treatment. Comparing the first columns of Figures E2 and E3 gives insight into the composition sensitivity of the IMs, since the d90 composition is heavier than that of SH*.

E.2. More Cases

Table E1 summarizes the results of additional cases to those listed in Table 1. For cases SH*, SH_E*, and SH_Q*, the best-fit parameters of the model are found by maximizing the

likelihood L (Equation (2)) for each assumption of HIM. The result leads to a composition that matches Sibyll2.3 c the best for all three cases. To investigate what would be the likelihood to fit the anisotropy data with a UHECR composition inferred from the X_{\max} measurement with QGSJETII-04, we considered case SH_{forceQ}*, where we maximize $\ln L(\langle \ln A \rangle | \Omega; \text{HIM}) + \ln L(\sigma^2(\ln A) | \Omega; \text{HIM})$ with composition parameter Ω first and then maximize $\ln L(\text{dipole} | \Theta; \text{source}) + \ln L(\text{events} | \Theta; \text{source})$, varying the other two parameters $D_{\text{EG},5\text{EeV}}$ and λ_G . Evidently, the fit to the anisotropy with a light composition is quite poor. The strength of the predicted LSS hot spot for our best-fitting description,

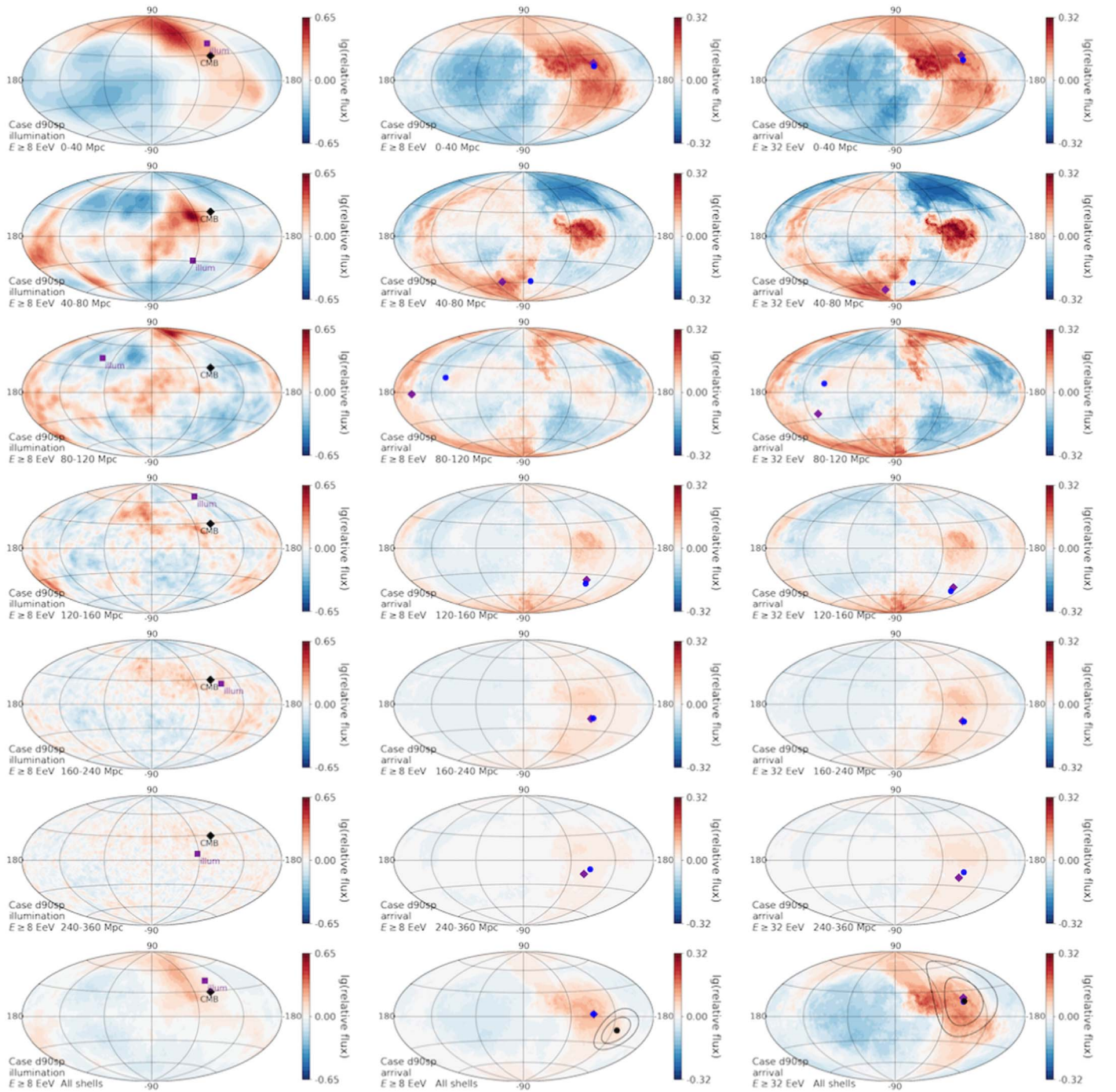


Figure E3. IMs (UHECR flux illuminating the Galaxy) and arrival maps (after propagation in the JF12 GMF model) for the model case d90sp and energy bins ≥ 8 and ≥ 32 EeV for different shells of distances.

case SH^{*}, is weaker than the one observed. This could be the result of fitting to the arrival directions of all events above 38 EeV, which contains more information than just the strength of the hot spot, including the shape of the hot spot and the south pole excess. To see whether a variation of the model parameters can give a similarly significant hot spot as observed, we carried out the exercise reported as case SH (Better Hot Spot)^{*}, for which the objective function also includes the number of events inside the hot spot. The conclusion is that the hot spot can indeed be readily described if it is included in the fitting, without significant damage to the fit to dipole components and events above 38 EeV.

E.3. Dipole and Quadrupole Components

Table E2 compares the dipole and quadrupole components of the LSS model arrival map ≥ 8 EeV with the Auger observation (Aab et al. 2018a, 2020a; di Matteo et al. 2020)

E.4. Mock Data Sets above 38 EeV

By simulating mock Auger data sets for the LSS model with a sharp cutoff (case SH^{*}) and for an isotropic sky (case Iso), we obtain the distribution of test statistics shown in Figure E5. The test statistic $TS = 2 \ln L(\text{events}|\Theta; \text{source}) = 22.1$, while the isotropic model is disfavored against the LSS sharp-cutoff

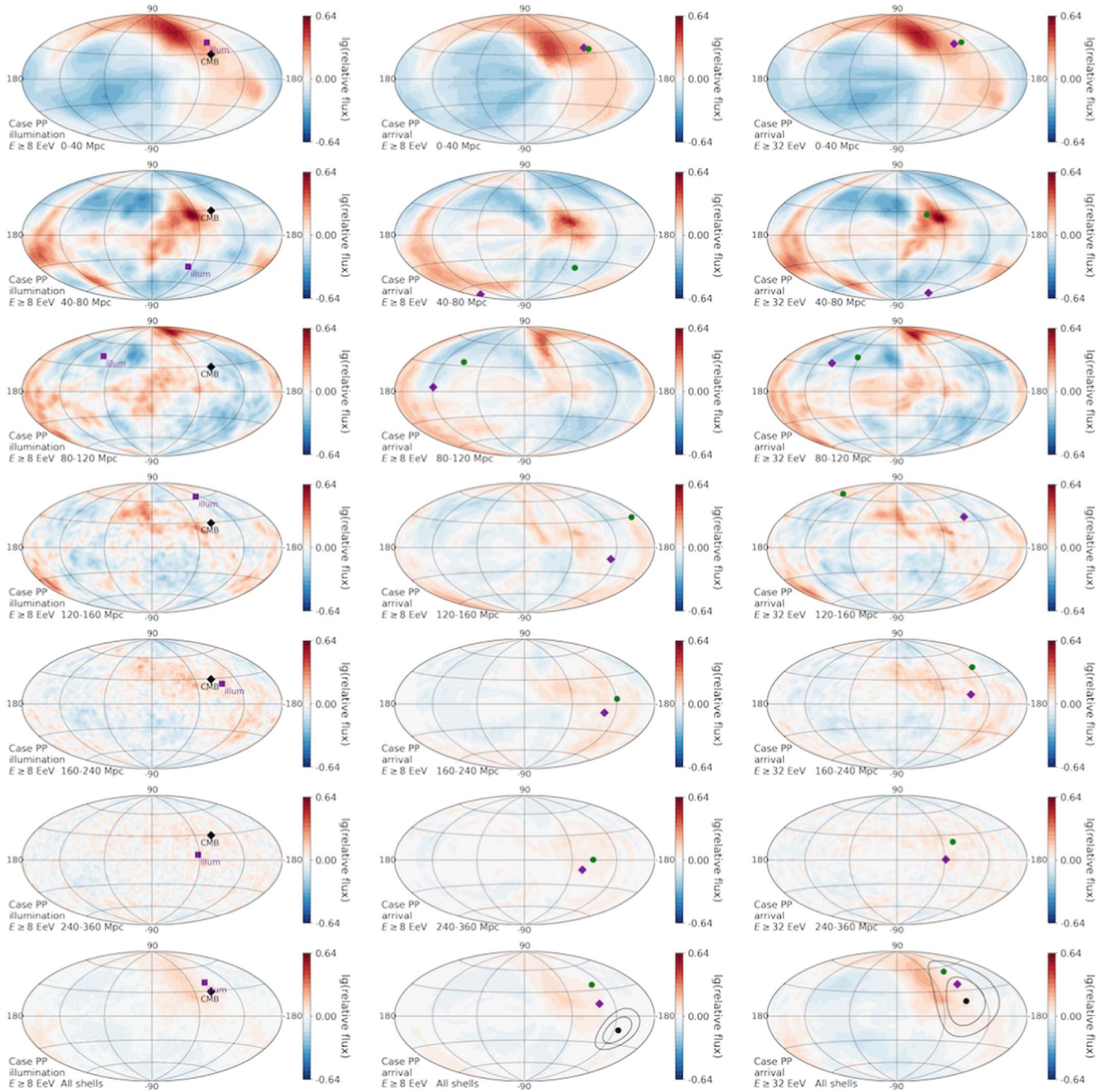


Figure E4. IMs (UHECR flux illuminating the Galaxy) and arrival maps (after propagation in the JF12 GMF model) for the model case PP and energy bins ≥ 8 and ≥ 32 EeV for different shells of distances.

model by 4.8σ . This is to be compared to Aab et al. (2018b), who found that the events above 39 EeV are correlated with a starburst galaxy catalog with $TS = 24.9$ and 4.0σ significance.

E.5. Corner Plots of Parameters

Figure E6 completes Table 1 and shows the corner plot of the probability distribution of parameters, assuming Sibyll2.3 c as the HIM. The 1D histograms on the diagonal show the probability distribution of each individual parameter

marginalized over the other five parameters. The 2D histograms off-diagonal show the probability distribution of two parameters marginalized over the other four parameters.

E.6. Result with Pure Proton Composition

As shown in Table 1, case E, the pure proton composition gives a much poorer fit to the anisotropy than case SH*. As illustrated in Figure E7, it gives a bad fit to dipole anisotropy ≥ 8 EeV. The arrival map ≥ 8 EeV has an excess in the northern

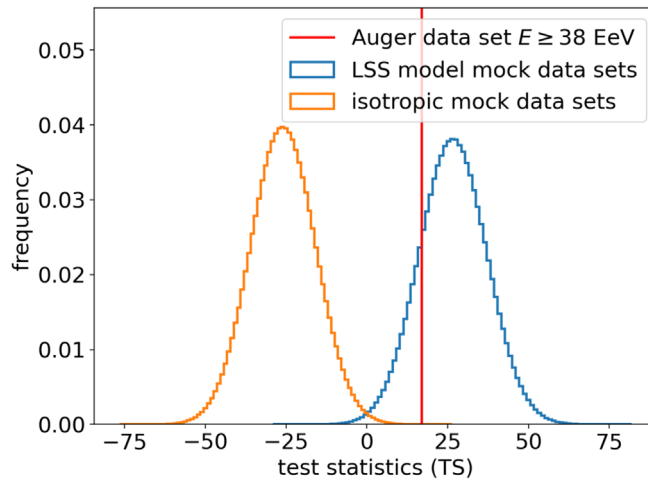


Figure E5. Test statistics of model mock data sets, isotropy mock data sets, and the Auger data set.

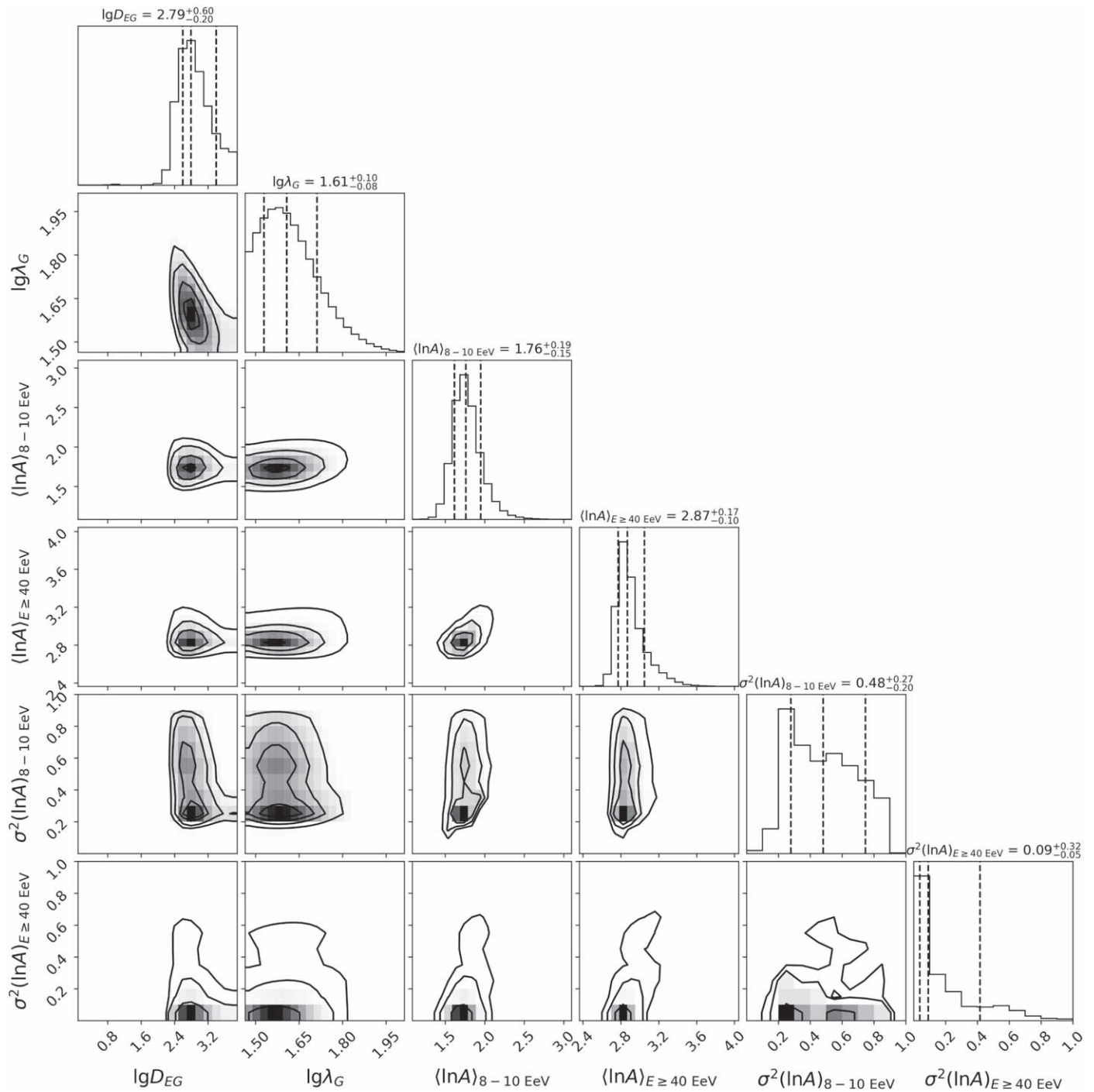


Figure E6. Corner plot of the probability distribution of parameters assuming Sibyll2.3 c as the HIM and using the sharp-cut-off treatment (case SH*).

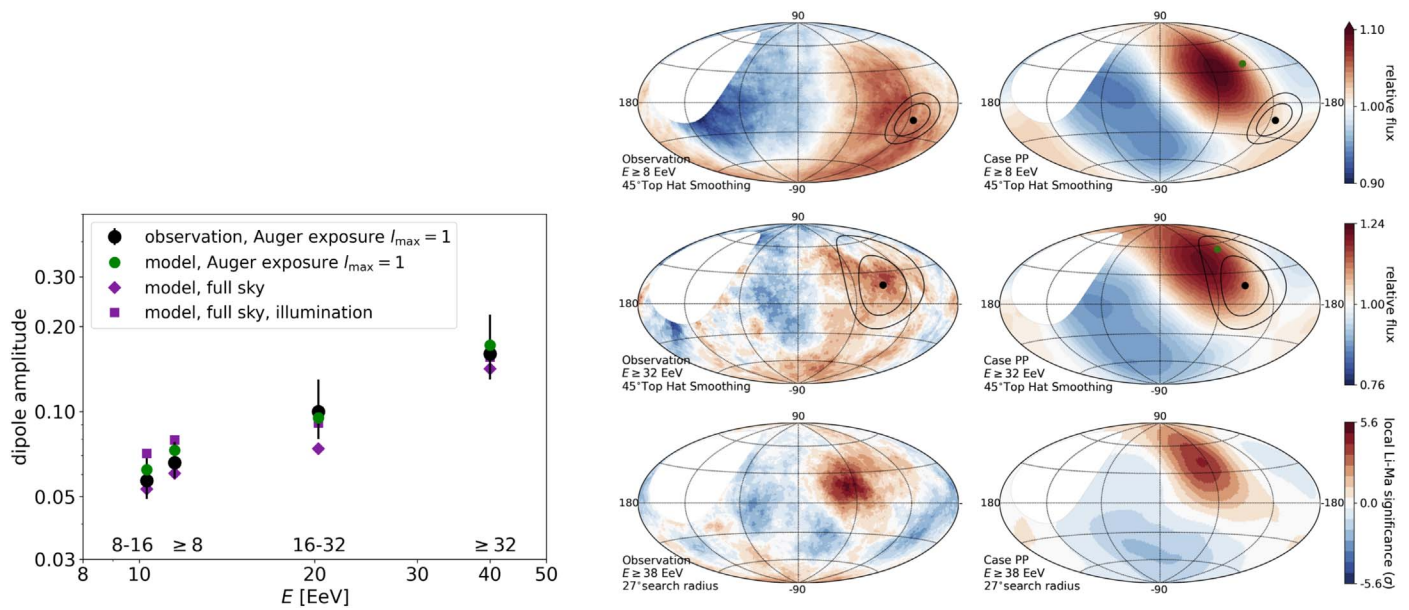


Figure E7. Sky maps for the pure proton composition with exponential cutoff (case PP) in the same format as Figure 4.

hemisphere, in contrast to the observation (Aab et al. 2017a). The small electric charge of the proton makes it impossible to be largely deflected by the GMF, which occurs for the actual mixed composition. Ahlers et al. (2018), using a simplified treatment, also concluded that PP composition is disfavored.

ORCID iDs

Chen Ding (丁忱) <https://orcid.org/0000-0002-6898-4427>
 Noémie Globus <https://orcid.org/0000-0001-9011-0737>
 Glennys R. Farrar <https://orcid.org/0000-0003-2417-5975>

References

- Aab, A., Abreu, P., Aglietta, M., et al. 2017a, *Sci*, 357, 1266
 Aab, A., Abreu, P., Aglietta, M., et al. 2017b, *JCAP*, 04, 038
 Aab, A., Abreu, P., Aglietta, M., et al. 2018a, *ApJ*, 868, 4
 Aab, A., Abreu, P., Aglietta, M., et al. 2018b, *ApJL*, 853, L29
 Aab, A., Abreu, P., Aglietta, M., et al. 2020a, *ApJ*, 891, 142
 Aab, A., Abreu, P., Aglietta, M., et al. 2020b, *PhRvL*, 125, 121106
 Aab, A., Abreu, P., Aglietta, M., et al. 2020c, *PhRvD*, 102, 062005
 Abbasi, R., Abe, M., Abu-Zayyad, T., et al. 2018, *ApJL*, 867, L27
 Abbasi, R. U., Abuzayyad, T., Amman, J., et al. 2005, *PhLB*, 619, 271
 Abraham, J., Aglietta, M., Aguirre, I. C., et al. 2004, *NIMPA*, 523, 50
 Ahlers, M., Denton, P., & Rameez, M. 2018, *Proc. ICRC (Busan)*, 35, 282
 Allard, D. 2012, *APh*, 39-40, 33
 Allard, D., Ave, M., Busca, N., et al. 2006, *JCAP*, 09, 005
 Allard, D., Parizot, E., Khan, E., Goriely, S., & Olinto, A. V. 2005, *A&A*, 443, L29
 Alves Batista, R., Boncioli, D., di Matteo, A., van Vliet, A., & Walz, D. 2015, *JCAP*, 10, 063
 Biteau, J., Bister, T., Caccianiga, L., et al. 2019, *EPJWC*, 210, 01005
 Caccianiga, L. 2019, *Proc. ICRC (Madison, WI)*, 36, 206
 Chandrasekhar, S. 1960, *Radiative Transfer* (New York: Dover)
 Courtois, H. M., Pomarède, D., Tully, R. B., Hoffman, Y., & Courtois, D. 2013, *AJ*, 146, 69
 Deligny, O. 2016, *Proc. ICRC (The Hague)*, 34, 395
 di Matteo, A., Bister, T., Biteau, J., et al. 2020, *Proc. ICRC (Madison, WI)*, 36, 439
 Durrer, R., & Neronov, A. 2013, *A&AR*, 21, 62
 Farrar, G. R. 2014, *CRPhy*, 15, 339
 Farrar, G. R., & Sutherland, M. S. 2019, *JCAP*, 05, 004
 Globus, N., Allard, D., & Parizot, E. 2008, *A&A*, 479, 97
 Globus, N., Ding, C., & Farrar, G. R. 2019a, *Proc. ICRC (Madison, WI)*, 36, 243
 Globus, N., & Piran, T. 2017, *ApJL*, 850, L25
 Globus, N., Piran, T., Hoffman, Y., Carlesi, E., & Pomarède, D. 2019b, *MNRAS*, 484, 4167
 Gorski, K., Hivon, E., Banday, A., et al. 2005, *ApJ*, 622, 759
 Greisen, K. 1966, *PhRvL*, 16, 748
 Hayashida, N., Honda, K., Honda, M., et al. 1996, *PhRvL*, 77, 1000
 Henyey, L. G., & Greenstein, J. L. 1941, *ApJ*, 93, 70
 Hoffman, Y., Carlesi, E., Pomarède, D., et al. 2018, *NatAs*, 2, 680
 Jansson, R., & Farrar, G. R. 2012, *ApJ*, 757, 14
 Kawai, H., Yoshida, S., Yoshii, H., et al. 2008, *NuPhB*, 175, 221
 Kawata, K., di Matteo, A., Fujii, T., et al. 2020, *Proc. ICRC (Madison, WI)*, 36, 310
 Khan, E., Goriely, S., Allard, D., et al. 2005, *Aph*, 23, 191
 Kotera, K., & Lemoine, M. 2008, *PhRvD*, 77, 123003
 Li, T. P., & Ma, Y. Q. 1983, *ApJ*, 272, 317
 Linsley, J. 1963, *PhRvL*, 10, 146
 Muzio, M. S., Unger, M., & Farrar, G. R. 2019, *PhRvD*, 100, 103008
 Narasimhan, S. G., & Nayar, S. K. 2003, in *IEEE Conf. Proc. Computer Society Conference on Computer Vision and Pattern Recognition* (New York: IEEE), I-1
 Planck Collaboration, Aghanim, N., Alves, M. I. R., et al. 2016, *A&A*, 596, A105
 Pomarède, D., Tully, R. B., Graziani, R., et al. 2020, *ApJ*, 897, 133
 Rachen, J. P. 1996, PhD thesis, Rheinische Friedrich-Wilhelms-Universität Bonn
 Tully, R. B., Courtois, H., Hoffman, Y., & Pomarède, D. 2014, *Natur*, 513, 71
 Tully, R. B., Courtois, H. M., Dolphin, A. E., et al. 2013, *AJ*, 146, 86
 Unger, Farrar 2019, *EPJWC*, 210, 04005
 Waxman, E., Fisher, K. B., & Piran, T. 1997, *ApJ*, 483, 1
 Yushkov, A. 2019, *Proc ICRC (Madison, WI)*, 36, 482
 Zatsepin, G., & Kuzmin, V. 1966, *JETPL*, 4, 78
 Zonca, A., Singer, L., Lenz, D., et al. 2019, *JOSS*, 4, 1298